

# Localization of Dirac modes in finite-temperature $\mathbb{Z}_2$ gauge theory on the lattice

György Baranka\* and Matteo Giordano†

ELTE Eötvös Loránd University,  
Institute for Theoretical Physics,  
Pázmány Péter sétány 1/A, H-1117, Budapest, Hungary

## Abstract

We study the localization properties of the eigenmodes of the staggered Dirac operator in finite-temperature  $\mathbb{Z}_2$  pure gauge theory on the lattice in 2+1 dimensions. We find that the low modes turn from delocalized to localized as the system crosses over from the confined to the deconfined phase in the “physical” sector (positive average Polyakov loop) selected by external fermionic probes, while they remain delocalized in the “unphysical” sector (negative average Polyakov loop). This confirms that the close connection between deconfinement and localization of the low Dirac modes in the physical sector, already observed in other models, holds also in the simplest gauge theory displaying a deconfinement transition. We also observe a clear correlation of localized modes with fluctuations of the Polyakov loop away from the ordered value, as expected according to the “sea/islands” picture of localization, and with clusters of negative plaquettes. A novel finding is the presence of localized modes at the high end of the Dirac spectrum in all phases/sectors of the theory.

## 1 Introduction

In the imaginary-time functional-integral formulation of gauge theories at finite temperature, the effects of dynamical fermions are entirely encoded in the Euclidean Dirac operator in a gauge-field background. The properties of the spectrum of the Euclidean Dirac operator play an important role in various nonperturbative aspects of QCD and other gauge theories, including, e.g., the fate of chiral symmetry [1] and of the  $U(1)_A$  anomaly [2–4], and anomalous dimensions in conformal gauge theories [5]. More generally, eigenvalues and eigenvectors of the Euclidean Dirac operator probe the background gauge configuration in a nontrivial way, even in the absence of dynamical fermions.

In recent years it has become apparent that there is a close relation between the localization properties of the low-lying Dirac modes and the confining properties of gauge

---

\*barankagy@caesar.elte.hu

†giordano@bodri.elte.hu

theories. It is by now fairly well established, by means of numerical calculations on the lattice, that in the high-temperature phase of QCD the low-lying Dirac modes become localized [6–10] on the scale of the inverse temperature [7, 9], up to a temperature-dependent point in the spectrum [7, 10]. The same situation is also found in the high-temperature phase of other gauge theories [11–21] and gauge-theory related models [22–26]. This phenomenon has been put into a relation with the ordering of the Polyakov loops in the high-temperature phase [16, 23, 24], or more precisely with the presence of disorder in the form of local fluctuations of the Polyakov loop away from its ordered value. In what has been named the “sea/islands” picture of localization, the Polyakov loop fluctuations provide “energetically” favorable “islands” for the modes to localize in the middle of a “sea” of ordered Polyakov loops. Clear numerical evidence of the correlation between localized modes and Polyakov loop fluctuations has been presented in the literature, for staggered and overlap spectra in quenched SU(2) gauge theory [16], and for overlap spectra in the background of SU(3) gauge fields with dynamical domain wall fermions [9] and twisted-mass Wilson fermions [10] (although with heavier-than-physical pions).

Localization of eigenmodes induced by disorder is a well-studied phenomenon in condensed matter physics, dating back to the groundbreaking work of Anderson [27]. In the language of condensed matter, disorder leads to the spatial localization of eigenmodes in certain spectral regions, separated by so-called “mobility edges” from regions where modes are delocalized. Extensive work has led to a thorough understanding of localization, in particular concerning its aspects at criticality (see, e.g., Refs. [28–31]). Detailed numerical studies have confirmed that localization of the low-lying Dirac modes in QCD at high temperature  $T$  shares the same critical features with three-dimensional Hamiltonians with on-site disorder in the appropriate symmetry class [8, 32, 33]. This provides evidence in support of the conjectured connection between localized modes and Polyakov loop fluctuations, that have the right properties to be the relevant source of disorder.<sup>1</sup>

Further insight was obtained in Ref. [24], using an explicit representation of the staggered lattice Dirac operator as a set of coupled Anderson models, with random on-

---

<sup>1</sup>In a three-dimensional Anderson model with uncorrelated purely off-diagonal logarithmically-distributed disorder in the chiral unitary class, García-García and Cuevas [34] found that the amount of off-diagonal disorder required to achieve localization at the band center is much larger than what is available in QCD. This suggests that on-site disorder (from the spatial, three-dimensional point of view) is needed to explain localization of the low modes in QCD, and Polyakov loops match the description. Interestingly, however, similar results were obtained by Takaishi *et al.* [35] for an Anderson model with purely off-diagonal but correlated disorder in the three-dimensional chiral unitary class, where they found the same critical statistics as in QCD. It is worth mentioning that while the Dirac operator in finite-temperature QCD belongs to the three-dimensional *chiral* unitary class, the critical behavior is expected to match that of the non-chiral class when the Anderson transition is away from the origin. This is confirmed by results for the correlation-length critical exponent [8], the critical statistics [8, 32] and the multifractal exponents [33]. Near the origin, instead, Ref. [34] found multifractal exponents different from those of the corresponding non-chiral class. Recently, the Anderson transition at the origin was studied in a chiral unitary model with on-site disorder in Ref. [36], that found a correlation length critical exponent different from the one pertaining to the non-chiral class.

site potential related to the phases of the untraced Polyakov loops. There it was pointed out that besides the presence of disorder in the form of Polyakov loop fluctuations, an important role in the appearance of localized low modes is played by the presence of strong correlations of gauge fields in the temporal direction. Temporal correlations in fact lead to the decoupling of the various Anderson models, and this makes localization of the low modes possible. While Polyakov loop fluctuations are present also at low  $T$  (although there the spatial average of the Polyakov loop is close to zero), temporal correlations are induced by the ordering of the Polyakov loops and so are specific to the high- $T$  phase.

Perhaps the most interesting aspect of the sea/islands picture is its simplicity: all that it requires is the presence of order in the Polyakov loop configuration, inducing strong temporal correlations on the one hand, and providing spatially localized fluctuations away from the ordered value on the other. This suggests that all that is required for localized low Dirac modes to appear is the existence of a deconfined phase of the theory, irrespectively of the dimensionality of the system<sup>2</sup> or the nature of the gauge group. This idea has since been investigated in several models, including pure-gauge SU(3) in 3+1 [18, 20] (see also Refs. [6, 11, 12] for older results) and 2+1 [19] dimensions, a lattice toy model of QCD with unimproved staggered fermions on  $N_t = 4$  lattices [17], a QCD-inspired spin model [24, 25], the CP<sup>3</sup> model in 2+1 dimensions [26], and recently in trace-deformed SU(3) gauge theory in 3+1 dimensions [21]. Results were already available in the case of the SU(2) theory in 3+1 dimensions [14, 15], two-flavor QCD [13], and the Instanton Liquid Model for QCD of Ref. [22]. In all these cases localized low modes have been found in the deconfined phase of the theory. Detailed studies of SU(3) gauge theory in 3+1 [18, 20] and 2+1 dimensions [19], as well as of the QCD toy model with unimproved fermions [17], the QCD-inspired spin model of Ref. [25], and of trace-deformed SU(3) gauge theory [21], have found convincing evidence that localization appears precisely at the deconfinement transition. All these findings strongly support the existence of a very close connection between localization of the low-lying Dirac modes and deconfinement.

The purpose of this work is to push the localization/deconfinement connection to its limit by studying the simplest lattice gauge theory displaying a finite-temperature deconfining transition:  $\mathbb{Z}_2$  pure gauge theory in 2+1 dimensions [37–39]. This is the simplest possible gauge group, and the lowest dimension where a deconfining transition is found. Furthermore, due to the discrete nature of the gauge group, there are no instanton-related topological aspects of the gauge configurations to take into account, that have been shown to strongly affect the low end of the spectrum in SU(3) gauge theory in 3+1 dimensions [40].

It is worth at this point clarifying in what sense an Anderson transition can take place in the spectrum of the Dirac operator (or more precisely, of a suitable lattice

---

<sup>2</sup>An exception are 1+1 dimensional systems: only localized modes are in fact expected in (spatially) one-dimensional disordered systems, for any amount of disorder (see Refs. [28, 29] and references therein). This is the case for the 1+1 dimensional CP<sup>3</sup> model at finite temperature, also studied in Ref. [26], where only localized modes are found in both phases of the model.

discretization thereof) when one is dealing with a pure gauge theory. The following discussion focuses on  $\mathbb{Z}_2$  lattice gauge theory, but can be adapted to any gauge theory with a non-trivial center symmetry (see below Section 2). In the high-temperature phase of these theories center symmetry is broken, and degenerate but inequivalent ground states exist with non-vanishing Polyakov-loop expectation value aligned to one of the center elements. To select a ground state, the standard procedure is to introduce a small symmetry-breaking perturbation in the finite-volume system, that lifts the degeneracy, and in the thermodynamic limit suppresses all but one of the (would-be) ground states. After this limit is taken the perturbation is removed, and the desired unperturbed ground state is selected. In contrast, in the low-temperature unbroken phase the unique ground state is always recovered after this procedure.

In the system at hand, such a perturbation is provided by very heavy but otherwise perfectly physical fermion fields, coupled to the gauge fields via the (suitably discretized) Dirac operator. These modify the weight of the gauge configurations in the partition function, preferring configurations with positive spatially-averaged Polyakov loop, thus selecting the “physical” positive center sector, and the corresponding (slightly perturbed) ground state in the thermodynamic limit.<sup>3</sup> The perturbation is then removed by making the fermions static, i.e., by taking the infinite-mass, quenched limit resulting in pure gauge theory. Preference for the physical center sector of course persists if dynamical (non-static) fermions are instead kept in the theory, in which case center symmetry is broken explicitly. Similarly, introducing unphysical pseudofermion fields, i.e., spin- $\frac{1}{2}$  commuting fields again coupled to the gauge fields through the Dirac operator, configurations with negative spatially-averaged Polyakov loop are preferred, thus selecting the “unphysical” negative center sector.<sup>4</sup>

The static fields discussed above can also be used to probe the system across the deconfinement transition, by studying the eigenmodes of the Dirac operator in the background of the relevant gauge configurations. In general, the transition looks different to different types of probes, which see the system transition from the confined phase at low temperature to the deconfined phase in a specific center sector at high temperature. How the localization properties of the modes change across the transition, and whether an Anderson transition appears in the spectrum, can depend on the probe being used, i.e., on the center sector selected in the high-temperature phase. According to the sea/islands picture, such an Anderson transition is expected to take place in the physical sector selected by fermion probes, but not in the unphysical sector selected by pseudofermion

---

<sup>3</sup> A positive (resp. negative) spatially-averaged Polyakov loop correlates with a lower (resp. higher) density of low modes. Since fermions (resp. pseudofermions) modify the weight that gauge configurations have in the pure gauge theory by a factor equal to the determinant (resp. inverse of the determinant) of the Dirac operator plus the mass, the positive (resp. negative) center sector is preferred when they are included in the dynamics. This is demonstrated explicitly for  $SU(2)$  gauge fields, see, e.g., Ref. [41]. We will show that this is the case also for  $\mathbb{Z}_2$  fields when discussing the spectral density of the staggered Dirac operator in Section 4.2.

<sup>4</sup>Another way to select a nontrivial center sector, which can be applied also to  $SU(N_c)$  theories, is to introduce a suitable imaginary chemical potential for the fermions.

probes. In fact, islands of negative Polyakov loops in a sea of positive Polyakov loops, as found in the physical sector, are needed for localization to take place, while in the opposite case found in the unphysical sector one expects an even stronger delocalization on the favorable sea of negative Polyakov loops.

From the discussion above, it is clear that the sea/islands picture leads to expect specific correlations between the low modes and the local properties of the gauge configurations, in particular the local orientation of the Polyakov loops, which are therefore worth investigating. This is particularly important in the light of the strong connection between low-mode localization and deconfinement implied by this picture. Indeed, establishing the correctness of the sea/islands picture of localization would allow to attack the problem of confinement from a new perspective, possibly leading to a better understanding of the microscopic mechanism that underlies confinement and the deconfinement transition.

The plan of the paper is the following. In Section 2 we briefly review the relevant aspects of  $\mathbb{Z}_2$  lattice gauge theory. In Section 3 we discuss how to detect localization of Dirac eigenmodes, and which observables to use in order to study the correlation between localization and various properties of the gauge field configuration. In Section 4 we show our numerical results. Finally, in Section 5 we present our conclusions and outlook for future studies. Technical details concerning the treatment of degenerate modes are discussed in Appendix A.

## 2 $\mathbb{Z}_2$ lattice gauge theory

The dynamical variables of  $\mathbb{Z}_2$  gauge theory on a hypercubic lattice are the link variables  $U_\mu(n) = \pm 1$ , taking values in  $\mathbb{Z}_2$ , associated to the oriented lattice links connecting site  $n$  with its neighbors  $n + \hat{\mu}$ . In 2+1 dimensions  $n = (n_1, n_2, n_3) = (t, \vec{x})$ , where  $0 \leq t = n_1 \leq N_t - 1$ ,  $0 \leq x_{1,2} = n_{2,3} \leq N_s - 1$ , and  $\hat{\mu}$  is the unit lattice vector in direction  $\mu$ , with  $\mu = 1, 2, 3$ . Periodic boundary conditions are imposed in all directions. The Wilson action for the  $\mathbb{Z}_2$  gauge theory reads (up to an irrelevant additive constant)

$$S[U] = -\beta \sum_n \sum_{\substack{\mu, \nu=1 \\ \mu < \nu}}^3 U_{\mu\nu}(n), \quad (1)$$

where the plaquette variables  $U_{\mu\nu}$  read simply  $U_{\mu\nu}(n) = U_\mu(n)U_\nu(n + \hat{\mu})U_\mu(n + \hat{\nu})U_\nu(n)$ , and  $\beta = 1/(e^2 a)$  with  $e$  the coupling constant (of mass dimension 1/2) and  $a$  the lattice spacing. Expectation values are defined as

$$\langle O[U] \rangle = Z^{-1} \sum_{\{U_\mu(n)=\pm 1\}} e^{-S[U]} O[U], \quad Z = \sum_{\{U_\mu(n)=\pm 1\}} e^{-S[U]}, \quad (2)$$

where  $Z$  is the partition function and the sum is over all possible gauge configurations. The finite-temperature case is studied by taking the thermodynamic limit  $N_s \rightarrow \infty$  at

fixed  $N_t$ , and varying  $\beta$ . In this approach  $\beta$  can be identified with the temperature  $T = 1/(aN_t)$  of the system,  $T/e^2 = \beta/N_t$  (we ignore scaling violations for simplicity).

The phase diagram of the  $\mathbb{Z}_2$  gauge model has been studied in detail in Ref. [42] exploiting the duality relation with the three-dimensional Ising model. A second-order phase transition takes place at a critical  $\beta_c = \beta_c(N_t)$ , separating a confined phase at  $\beta < \beta_c$  from a deconfined one at  $\beta > \beta_c$ . Deconfinement is signaled by the spontaneous breaking of the center symmetry of the model, i.e., the symmetry under the transformation

$$U_1(N_t - 1, \vec{x}) \rightarrow z U_1(N_t - 1, \vec{x}) \quad \forall \vec{x}, \quad z \in \mathbb{Z}_2, \quad (3)$$

with  $z$  an element of the group center (which for an Abelian group coincides with the group itself). The relevant order parameter is the expectation value,  $\langle P(\vec{x}) \rangle$ , of the Polyakov loop,

$$P(\vec{x}) \equiv \prod_{t=0}^{N_t-1} U_1(t, \vec{x}). \quad (4)$$

In the thermodynamic limit, this vanishes in the confined phase, while it is nonzero in the deconfined phase where the Polyakov loop gets ordered, taking mostly either the  $+1$  or the  $-1$  value, depending on the choice of ground state. This choice is made in practice already in a finite volume, by selecting configurations with the desired sign of the spatially-averaged Polyakov loop,  $\bar{P} \equiv V^{-1} \sum_{\vec{x}} P(\vec{x})$ , where  $V = N_s^2$  is the lattice spatial volume. Here and in the following all quantities are expressed in lattice units, unless explicitly stated otherwise. We will refer to configurations with positive  $\bar{P}$  as belonging to the physical sector, and to those with negative  $\bar{P}$  as belonging to the unphysical sector. As already explained in the Introduction, the reason for this nomenclature is that these configurations are favored respectively by dynamical fermion or pseudofermion fields, and in the spontaneously broken phase they are strictly selected after the thermodynamic limit is taken. Restricting to one sector provides an accurate approximation of the partition function in the broken phase for large enough volumes, while both sectors must always be included in the unbroken phase.

In this paper we study the spectrum of the staggered Dirac operator in the background of quenched  $\mathbb{Z}_2$  configurations, thus probing the gauge fields with external fermion or pseudofermion fields. In the case at hand, the staggered operator reads

$$D_{n,n'}^{\text{stag}} = \frac{1}{2} \sum_{\mu=1}^3 \eta_{\mu}(n) (U_{\mu}(n) \delta_{n+\hat{\mu},n'} - U_{\mu}(n - \hat{\mu}) \delta_{n-\hat{\mu},n'}), \quad (5)$$

$$\eta_{\mu}(n) = (-1)^{\sum_{\nu < \mu} n_{\nu}},$$

with periodic boundary conditions in the spatial directions and antiperiodic boundary conditions in the temporal direction. The operator  $D^{\text{stag}}$  is anti-Hermitian and so has purely imaginary eigenvalues,

$$D^{\text{stag}} \psi_l = i \lambda_l \psi_l, \quad \lambda_l \in \mathbb{R}. \quad (6)$$

The staggered operator satisfies furthermore the chiral property  $\{\varepsilon, D^{\text{stag}}\} = 0$ , where  $\varepsilon(n) = (-1)^{\sum_{\mu=1}^3 n_{\mu}}$ , which implies

$$D^{\text{stag}}\varepsilon\psi_l = -i\lambda_l\varepsilon\psi_l, \quad (7)$$

so that the spectrum is symmetric about zero.

In the continuum limit,  $D^{\text{stag}}$  describes  $N_f = 4$  degenerate species of fermions also in 2+1 dimensions [43].<sup>5</sup> Here we do not attempt any extrapolation to the continuum limit and work at finite lattice spacing. In this case the staggered fermionic action in the massless limit,  $S^{\text{stag}} = \sum_{n,n'} \bar{\chi}(n) D^{\text{stag}}(n, n') \chi(n')$ , still retains an exact  $U(1)_1 \times U(1)_{\varepsilon}$  chiral symmetry [43] under the following transformations of the fermion fields  $\chi, \bar{\chi}$ :

$$\begin{aligned} U(1)_1 : \chi(n) &\rightarrow e^{i\alpha}\chi(n), & \bar{\chi}(n) &\rightarrow \bar{\chi}(n)e^{-i\alpha}, \\ U(1)_{\varepsilon} : \chi(n) &\rightarrow e^{i\alpha\varepsilon(n)}\chi(n), & \bar{\chi}(n) &\rightarrow \bar{\chi}(n)e^{i\alpha\varepsilon(n)}. \end{aligned} \quad (8)$$

The  $U(1)_{\varepsilon}$  symmetry can break down spontaneously by formation of a quark-antiquark condensate, signalled by a nonzero density of near-zero modes [1]. Although we are working in the opposite, “quenched” limit of infinitely massive fermions, it is nonetheless worth checking whether a nonzero density of near-zero modes is present in the thermodynamic limit.

### 3 Localization of Dirac eigenmodes

The simplest way to detect localization is to study the so-called *inverse participation ratio* (IPR) of the Dirac eigenmodes  $\psi_l$ ,

$$\text{IPR}_l \equiv \sum_n |\psi_l(n)|^4, \quad (9)$$

where it is understood that modes satisfy the normalization condition  $\sum_n |\psi_l(n)|^2 = 1$ . Since  $|\varepsilon(n)\psi_l(n)| = |\psi_l(n)|$ , one finds the same IPR for the eigenmodes corresponding to  $\lambda_l$  and  $-\lambda_l$ ; similar symmetry considerations hold for any observable built out of  $|\psi_l(n)|$ . It then suffices to consider only  $\lambda_l \geq 0$ .

For delocalized modes extended throughout the whole lattice, one has the qualitative behavior  $|\psi_{\text{ext}}(n)|^2 \sim (N_t V)^{-1}$ , and so  $\text{IPR}_{\text{ext}} \sim (N_t V)^{-1}$ , which vanishes in the large-volume limit. For modes localized in a region of spatial volume  $V_0$  one has instead approximately  $|\psi_{\text{loc}}(n)|^2 \sim (N_t V_0)^{-1}$  within that region and zero outside, and so  $\text{IPR}_{\text{loc}} \sim (N_t V_0)^{-1}$ , which remains finite as the volume increases. Equivalently, one can consider the *participation ratio* (PR) of the modes,

$$\text{PR}_l \equiv \text{IPR}_l^{-1} (N_t V)^{-1}, \quad (10)$$

---

<sup>5</sup>In Ref. [19] it is mistakenly stated  $N_f = 2$ .

which measures the fraction of spacetime that they effectively occupy, and as  $V \rightarrow \infty$  approaches a constant for extended modes, and zero for localized modes; or the “size” of the modes,  $\text{PR}_l \cdot N_t V = \text{IPR}_l^{-1}$ , which diverges like  $V$  for extended modes, and tends to a constant for localized modes.

To identify the spectral regions where modes are localized, one divides the support of the spectrum in small (ideally infinitesimal) bins, and averages, e.g., the PR of the modes within each bin and over gauge configurations,

$$\text{PR}(\lambda, N_s) \equiv \frac{\langle \sum_l \delta(\lambda - \lambda_l) \text{PR}_l \rangle}{\langle \sum_l \delta(\lambda - \lambda_l) \rangle}, \quad (11)$$

studying then the behavior of  $\text{PR}(\lambda, N_s)$  as  $N_s$  is changed at fixed  $\lambda$ . In practice, to estimate this quantity locally in the spectrum we divided the full spectral range in bins of small but finite width  $\Delta\lambda$ , did the averaging within each bin separately, and assigned the result to the average eigenvalue in the bin. The same procedure was used for the other observables considered in this work. At large  $N_s$  one expects the following scaling behavior of  $\text{PR}(\lambda, N_s)$ ,

$$\text{PR}(\lambda, N_s) \simeq c(\lambda) N_s^{\alpha(\lambda)-2}, \quad (12)$$

with some volume-independent  $c(\lambda)$ , and where  $\alpha(\lambda)$  is the fractal dimension of the eigenmodes in the given spectral region. For extended, fully delocalized modes one has  $\alpha = 2$ , while for localized modes  $\alpha = 0$ . The fractal dimension can then be extracted from pairs of different system sizes  $N_{s1,2}$  via

$$\alpha(\lambda) = 2 + \log \left( \frac{\text{PR}(\lambda, N_{s1})}{\text{PR}(\lambda, N_{s2})} \right) / \log \left( \frac{N_{s1}}{N_{s2}} \right), \quad (13)$$

for sufficiently large  $N_{s1,2}$ .

The presence and the nature of Anderson transitions in two-dimensional systems is a much more delicate issue than in the three-dimensional case. According to the scaling theory of localization [44], Anderson transitions are generally expected to be absent in two-dimensional disordered systems, and all modes are expected to be localized, except for the symplectic class (see Refs. [29, 30] for details and references). In practice, however, this issue strongly depends on the details of the system. The inclusion of topological effects in the field-theoretical description of localization (see Ref. [30] for references) allows the presence of Anderson transitions also in certain other symmetry classes (see Ref. [30] and references cited in Ref. [45]), in particular in the chiral classes [46]. Numerical results show that a second-order Anderson transition is present in the theory of the integer Quantum Hall Effect [47], in the two-dimensional unitary class. The critical behavior has been elucidated in terms of a marginally-perturbed conformal theory [48], which is supported by very recent numerical results [49]. An Anderson transition of BKT (Berezinskii-Kosterlitz-Thouless) type is instead present in the two-dimensional unitary Anderson model [45], which is in the same, non-chiral unitary class, and in SU(3) gauge theory in 2+1 dimension [19], which is in the two-dimensional chiral unitary class. An

Anderson transition is present also in the  $CP^3$  model in 2+1 dimensions [26], again in the two-dimensional chiral unitary class, while for the two-dimensional model with correlated, purely off-diagonal disorder studied in Ref. [35], in the same symmetry class, results are admittedly not conclusive. Finally, a transition of BKT type has been observed also in the orthogonal class, in a model for disordered graphene with strong long-range impurities mimicked by a suitable on-site random potential [50].

The random “Hamiltonian” of interest in this paper is  $H = -iD^{\text{stag}}$ , which has purely imaginary matrix elements and satisfies the chiral property  $\{\varepsilon, H\} = 0$ , and so is invariant under the anti-unitary transformation  $T = \varepsilon K$ , where  $K$  denotes complex conjugation,

$$THT^\dagger = \varepsilon H^* \varepsilon = -\varepsilon H \varepsilon = H. \quad (14)$$

Since  $T^2 = 1$  and  $[T, \varepsilon] = 0$ ,  $H$  belongs to the chiral orthogonal class [30, 51, 52]. Numerical studies of Anderson models in this class, employing bipartite lattices and purely off-diagonal disorder, have found that all non-zero energy modes are localized. The zero-energy point is singled out by chiral symmetry and critical modes are found there [53–56], that become localized for sufficiently strong disorder in certain models [57]. In the case at hand, however, an argument analogous to that of Refs. [16, 23, 24] shows how local fluctuations of the Polyakov loop effectively provide a two-dimensional on-site disorder. In analogy with what has been found for the  $SU(3)$  gauge theory [19], which is in the chiral unitary class but behaves similarly to the non-chiral unitary Anderson model [45], displaying a BKT-type Anderson transition at finite energy, we are then led to expect a behavior similar to that found in the above-mentioned model in the non-chiral orthogonal class [50]. We then expect to find a true Anderson transition in the spectrum of the Dirac operator in the physical sector of the deconfined phase of  $\mathbb{Z}_2$  gauge theory in 2+1 dimensions, and we expect it to be of BKT type. This means in particular that we do not expect to find a sudden transition from an “insulating” side (fractal dimension 0) to a “metallic” side (fractal dimension 2) when crossing the mobility edge. All points in the spectrum beyond the mobility edge are in fact expected to be critical, with nontrivial fractal properties of the corresponding eigenmodes, intermediate between insulating and metallic.

It is expected from the sea/islands picture of localization that localized modes correlate with the fluctuations of the Polyakov loop away from order. To study this correlation we have considered the following observable,

$$\mathcal{P}(\lambda) \equiv \frac{\langle \sum_l \delta(\lambda - \lambda_l) \sum_{t, \vec{x}} P(\vec{x}) |\psi_l(t, \vec{x})|^2 \rangle}{\langle \sum_l \delta(\lambda - \lambda_l) \rangle}, \quad (15)$$

i.e., the spatial average of the Polyakov loop weighted by the eigenmode density, or the “Polyakov loop seen by a mode” [16]. For fully delocalized modes one expects

$$\sum_{t, \vec{x}} P(\vec{x}) |\psi_l(t, \vec{x})|^2 \simeq \frac{1}{N_t V} \sum_{t, \vec{x}} P(\vec{x}) = \frac{1}{V} \sum_{\vec{x}} P(\vec{x}) = \bar{P}, \quad (16)$$

and so approximately  $\mathcal{P} \simeq \langle P \rangle$  in spectral regions where modes are extended. In the physical sector, localized modes are expected to prefer to live close to negative Polyakov loops, and so  $\mathcal{P}$  is expected to be considerably smaller than  $\langle P \rangle$ . Notice that  $\frac{1-\mathcal{P}(\lambda)}{2}$  measures exactly “how much” of the mode lives on sites corresponding to a negative Polyakov loop.

The dynamics of the  $\mathbb{Z}_2$  gauge theory can be trivially reexpressed in terms of clusters of negative plaquettes. As pointed out in Ref. [58], what is nontrivial is that at the deconfinement transition (in 2+1 dimensions) the largest such cluster ceases to scale like the system size, i.e., is not fully delocalized. It is then interesting to check whether there is correlation between localized modes and negative plaquettes. To do so we have used two different observables, namely

$$\mathcal{W}(\lambda) \equiv \frac{\langle \sum_l \delta(\lambda - \lambda_l) \sum_n A(n) |\psi_l(n)|^2 \rangle}{\langle \sum_l \delta(\lambda - \lambda_l) \rangle}, \quad (17)$$

and

$$\tilde{\mathcal{W}}(\lambda) \equiv \frac{\langle \sum_l \delta(\lambda - \lambda_l) \sum_{n, A(n) > 0} |\psi_l(n)|^2 \rangle}{\langle \sum_l \delta(\lambda - \lambda_l) \rangle}, \quad (18)$$

where  $A(n) \geq 0$  counts the number of negative plaquettes touching the lattice site  $n$ ,

$$A(n) \equiv \frac{1}{2} \sum_{\substack{\mu, \nu=1 \\ \mu < \nu}}^3 [4 - U_{\mu\nu}(n) - U_{\mu\nu}(n - \hat{\mu}) - U_{\mu\nu}(n - \hat{\nu}) - U_{\mu\nu}(n - \hat{\mu} - \hat{\nu})]. \quad (19)$$

$\mathcal{W}(\lambda)$  then measures the average number of negative plaquettes touched by the modes, while  $\tilde{\mathcal{W}}(\lambda)$  measures how much of the modes lives on sites touched by negative plaquettes. For delocalized modes one expects

$$\sum_n A(n) |\psi_l(n)|^2 \simeq \frac{1}{N_t V} \sum_n A(n), \quad (20)$$

and so approximately  $\mathcal{W} \simeq 6(1 - \langle U_{\mu\nu} \rangle)$  in spectral regions where modes are extended. Estimating the probability that  $A(n) > 0$ , needed to estimate  $\tilde{\mathcal{W}}$  for delocalized modes, is instead not so straightforward.

To study the shape of the eigenmodes in more detail we measured their inertia tensor in the center-of-mass frame, and identified the corresponding principal axes and moments of inertia. A slight complication is due to the fact that the system of interest, i.e., the “mass” distribution  $m(n) = |\psi_l(n)|^2$  of mode  $l$ , lives on a lattice with periodic boundary conditions, i.e., on a discrete torus. To identify the center of mass we followed Ref. [59]. Each direction is embedded in a two-dimensional plane as a circle of radius  $\frac{N_\mu}{2\pi}$ , where  $N_\mu$  is the linear size in direction  $\mu$ , with embedding coordinates  $(\xi_\mu, \zeta_\mu)$ ,

$$\begin{aligned} \xi_\mu &= N_\mu \cos \theta_\mu(n), & \zeta_\mu &= N_\mu \sin \theta_\mu(n), \\ \theta_\mu(n) &= \frac{2\pi n_\mu}{N_\mu}, & 0 &\leq n_\mu \leq N_\mu - 1. \end{aligned} \quad (21)$$

Since  $\sum_n m(n) = 1$ , the position of the center-of-mass in the plane is easily found to be

$$\begin{aligned}\bar{\xi}_\mu &= N_\mu \sum_n m(n) \cos \theta_\mu(n), \\ \bar{\zeta}_\mu &= N_\mu \sum_n m(n) \sin \theta_\mu(n).\end{aligned}\tag{22}$$

This is then projected back on the circle via  $\bar{\xi}_\mu = \bar{r} \cos \bar{\theta}_\mu$ ,  $\bar{\zeta}_\mu = \bar{r} \sin \bar{\theta}_\mu$ , with  $\bar{\theta}_\mu \in [0, 2\pi)$  and  $\bar{r}^2 = \bar{\xi}_\mu^2 + \bar{\zeta}_\mu^2$ . Finally, as long as  $\bar{r} \neq 0$ , the lattice coordinates of the center of mass are obtained as

$$\bar{n}_\mu = N_\mu \frac{\bar{\theta}_\mu}{2\pi}.\tag{23}$$

If  $\bar{r} = 0$ , i.e.,  $\bar{\xi}_\mu = \bar{\zeta}_\mu = 0$ , then the mass distribution is uniform in direction  $\mu$ , and any point can be treated as the center of mass. The inertia tensor is now defined as

$$\Theta_{\mu\nu} \equiv \sum_n m(n) \left[ \delta_{\mu\nu} \sum_\rho (n_\rho - \bar{n}_\rho)_P^2 - (n_\mu - \bar{n}_\mu)_P (n_\nu - \bar{n}_\nu)_P \right],\tag{24}$$

where the periodic coordinate difference  $(n_\mu - \bar{n}_\mu)_P$  is defined as<sup>6</sup>

$$(n_\mu - \bar{n}_\mu)_P = \begin{cases} n_\mu - \bar{n}_\mu & \text{if } |n_\mu - \bar{n}_\mu| < |N_\mu - n_\mu + \bar{n}_\mu|, \\ N_\mu - n_\mu + \bar{n}_\mu & \text{if } |n_\mu - \bar{n}_\mu| > |N_\mu - n_\mu + \bar{n}_\mu|. \end{cases}\tag{25}$$

From the eigenvalues  $\theta_1 \geq \theta_2 \geq \theta_3$  of  $\Theta_{\mu\nu}$  one can find out the approximate shape of the mode. There are three particularly interesting cases: i.)  $\theta_1 \approx \theta_2 > \theta_3$ : the mode is more extended in one direction than in the other two, which are instead approximately equal (elongated, prolate shape); ii.)  $\theta_1 > \theta_2 \approx \theta_3$ : the mode is less extended in one direction than in the other two, which are instead approximately equal (flattened, oblate shape); iii.)  $\theta_1 \approx \theta_2 \approx \theta_3$ : the mode is extended approximately in the same way in all directions (spherical shape). Since the temporal direction is singled out, it is also interesting to check the relative orientation of the principal axes of the mode,  $v_{1,2,3}$ , with the temporal direction. For a randomly oriented axis, one would find for the average of the absolute value of  $\cos \varphi_j = v_j \cdot \hat{1}$  the following result,

$$\langle |\cos \varphi_j| \rangle = \frac{1}{2\pi} \int_0^{2\pi} d\phi \int_0^{\frac{\pi}{2}} d\theta \sin \theta \cos \theta = \frac{1}{2}.\tag{26}$$

Values larger than 1/2 indicate that the corresponding principal axis prefers to be oriented closer to the temporal direction, while values smaller than 1/2 indicate that it prefers to lie closer to the spatial plane.

$N_s$	$\beta =$ 0.67, 0.68, 0.69, 0.70, 0.75, 0.76, 0.77	$\beta =$ 0.71, 0.72, 0.725, 0.73, 0.7325, 0.735, 0.7375, 0.74, 0.745
20	2000	4000
24	1000	2000
28	600	1500
32	500	1000

Table 1: Number of configurations (per center sector) for the various lattice sizes and values of  $\beta$ .

## 4 Numerical results

We performed numerical simulations in both phases of the  $\mathbb{Z}_2$  gauge theory on periodic  $N_t \times N_s^2$  cubic lattices with  $N_t = 4$  and  $N_s = 20, 24, 28, 32$ . We used  $\beta$  values in the range  $[0.67, 0.77]$  on both sides of the critical coupling, that for  $N_t = 4$  is  $\beta_c(N_t = 4) = 0.73107(2)$  [42]. Details about the  $\beta$  values and the accumulated statistics can be found in Table 1. Simulations were performed with a standard Metropolis algorithm. For each configuration we measured the spatially-averaged Polyakov loop  $\bar{P}$ , and depending on its sign we assigned the configuration to the physical sector ( $\bar{P} > 0$ ) or to the unphysical sector ( $\bar{P} < 0$ ). We then obtained a new configuration with the same Boltzmann weight but belonging to the opposite sector by changing the sign of all the temporal links on the last time slice. Such a configuration was stored separately, leaving the flow of the simulation undisturbed. For both configurations we then obtained all the eigenvalues and eigenvectors of the staggered Dirac operator, Eq. (5), using the LAPACK library [60]. We then studied the properties of the eigenmodes locally in the spectrum, dividing the full spectral range in bins of width  $\Delta\lambda = 0.05$ . Statistical errors were estimated with the jackknife method. The chiral property allowed us to restrict to  $\lambda_l \geq 0$  without any loss of information.

Degenerate eigenvalues show up in the spectrum, especially frequently (for some reason unknown to us) in the spectral region around  $\lambda_* \equiv \sqrt{3}/2$ , which corresponds to the square root of the average squared eigenvalue of the staggered Dirac operator.<sup>7</sup> This is probably a finite-size effect, as signalled by the fact that the amount of degenerate modes tends to decrease as the lattice size is increased. Nonetheless, it is clearly visible for the lattice sizes studied in this paper. For degenerate eigenspaces it is more appropriate to assign a single value of the IPR to the whole eigenspace. This is obtained by averaging over the eigenspace with the procedure discussed in Appendix A. For observables

<sup>6</sup>Since the center of mass is almost never located on a lattice site, the case in which one finds equal magnitudes for the coordinate differences obtained following the two possible routes on the torus is very unlikely to happen, and can be ignored. In this case, since neither route is preferred, both should contribute equally to the sum in Eq. (24), yielding a vanishing contribution to off-diagonal terms.

<sup>7</sup>In  $d$  dimensions, for link variables in an  $N$ -dimensional representation of the gauge group (and for  $N_t > 2$ ) one has  $-(D^{\text{stag}^2})_{nn} = \frac{d}{2}\mathbf{1}_N$ , and so  $(N_t V N)^{-1} \sum_l \lambda_l^2 = \frac{d}{2}$ .

measuring the correlation of the local density of the modes,  $|\psi_l(n)|^2$ , with local gauge observables, the result of this averaging procedure coincides with the simple average over any orthonormal basis of the degenerate eigenspace, and no particular treatment is therefore required.

The simplicity of the  $\mathbb{Z}_2$  gauge model allows one to obtain full spectra on lattices of moderately large size in a reasonably short time (e.g., 500 configurations for  $N_s = 32$  are analyzed in less than a day on a standard CPU). The precise determination of the mobility edge separating regions of delocalized modes from regions of extended modes, on the other hand, requires the use of large system sizes for which full diagonalization is impractical. Full diagonalization algorithms in fact typically scale with the matrix size  $N$  like  $N^3$ , so in our case like  $N_s^6$ , and the time required for the analysis quickly ceases to be reasonable. In this work we have preferred to obtain an overview of the localization properties of the modes throughout the whole spectrum, rather than focussing on the low end only, postponing the detailed study of the mobility edge to future work.

For all the observables considered in this paper we have studied the two center sectors separately. In the deconfined phase, where center symmetry is spontaneously broken, this provides physical results corresponding to the two possible choices for the ground state, formally following from the use of fermion ( $\bar{P} > 0$ ) or pseudofermion ( $\bar{P} < 0$ ) fields to probe the system. In the confined phase the center symmetry is instead unbroken and the two sectors should be combined together. Furthermore, in this phase  $\bar{P}$  is small on typical configurations, and one expects little difference between the two sectors. Nevertheless, it is informative to study the two sectors separately, in particular to check how they evolve as the critical coupling is approached.

For couplings close to  $\beta_c$  one expects large finite-size effects for the available lattice sizes, and the corresponding results are therefore not expected to represent accurately the behavior of the system in the thermodynamic limit. We nonetheless included them in our plots, and they seem qualitatively in line with the general trend.

#### 4.1 Participation ratio

Our numerical results for the “size” of the modes,  $\text{PR} \cdot N_t V = \text{IPR}^{-1}$ , are shown in Figs. 1, 2, and 3 for the physical sector, and in Figs. 4 and 5 for the unphysical sector, for several values of  $\beta$  both below and above  $\beta_c$ , and for all the available lattice sizes. In the same figures we also show the fractal dimension  $\alpha$ , computed locally in the spectrum using Eq. (13). Since the average eigenvalue in the various spectral bins fluctuates slightly for different  $N_s$ , it is understood that we compare the average PR in the same spectral bin. Statistical errors were estimated by linear propagation of the jackknife errors on  $\text{PR}(\lambda, N_s)$ .

In the confined phase the contributions of the two center sectors should be combined to obtain the correct result. This is shown in Fig. 6. We first discuss the results in the two sectors separately, and briefly comment on the combined result in the confined phase afterwards.

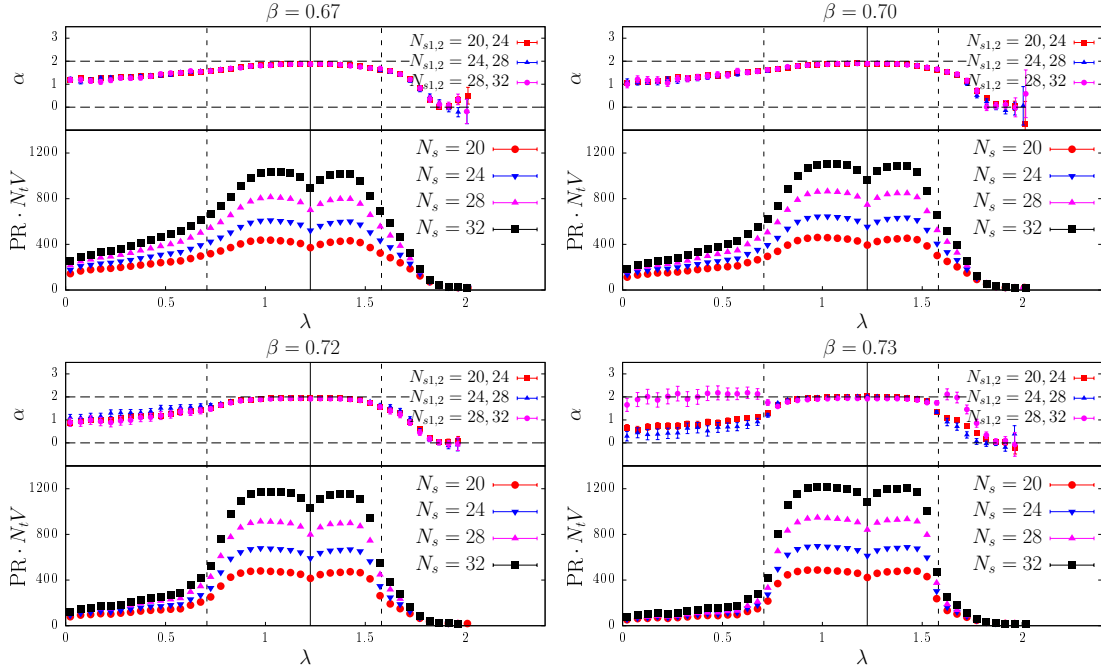


Figure 1: Confined phase, physical sector: mode size  $\text{PR} \cdot N_t V = \text{IPR}^{-1}$  (bottom panels) and fractal dimension  $\alpha$  (top panels). The points  $\lambda_{(0)}$ ,  $\lambda_*$  and  $\lambda_{(1)}$  (see Eq. (28)) are marked with vertical lines.

#### 4.1.1 Physical sector

The eigenvalues of the free staggered operator (i.e., on the trivial configuration  $U_\mu(n) = 1, \forall n, \mu$ ) in 2+1 dimensions read

$$\lambda_{\text{free}} = \pm \sqrt{(\sin \omega_k)^2 + (\sin p_1)^2 + (\sin p_2)^2}, \quad (27)$$

where  $\omega_k = \frac{(2k+1)\pi}{N_t}$ ,  $k = 0, \dots, N_t - 1$  are the Matsubara frequencies and  $p_j = \frac{2j\pi}{N_s}$ ,  $j = 0, \dots, N_s - 1$  are the lattice momenta. At fixed  $k$ , the positive eigenvalues lie in the ‘‘Matsubara sector’’  $[\sin \omega_k, \sqrt{\sin \omega_k^2 + 2}]$ ,  $k = 0, \dots, \frac{N_t}{2} - 1$  ( $k = \frac{N_t}{2}, \dots, N_t - 1$  are reserved instead for the negative spectrum), and so the whole positive spectrum lies in the interval  $[\sin \omega_0, \sqrt{\sin \omega_{\text{max}}^2 + 2}]$ , with  $\sin \omega_{\text{max}} = \max_k |\sin \omega_k|$ . For  $N_t = 4$  one has  $(\sin \omega_k)^2 = \frac{1}{2} \forall k$ . This suggests that one should distinguish three spectral regions in the physical sector: the low modes  $\lambda < \lambda_{(0)}$ , the bulk modes  $\lambda_{(0)} \leq \lambda \leq \lambda_{(1)}$ , and the high modes  $\lambda > \lambda_{(1)}$ , where

$$\lambda_{(0)} \equiv \sin \frac{\pi}{4} = \frac{1}{\sqrt{2}}, \quad \lambda_{(1)} \equiv \sqrt{(\sin \frac{\pi}{4})^2 + 2} = \sqrt{\frac{5}{2}}. \quad (28)$$

In both phases, the size of the mode,  $\text{IPR}^{-1}$ , is larger in the bulk than at the edges of the spectrum, as Figs. 1–3 (bottom panels) show. The volume scaling indicates that

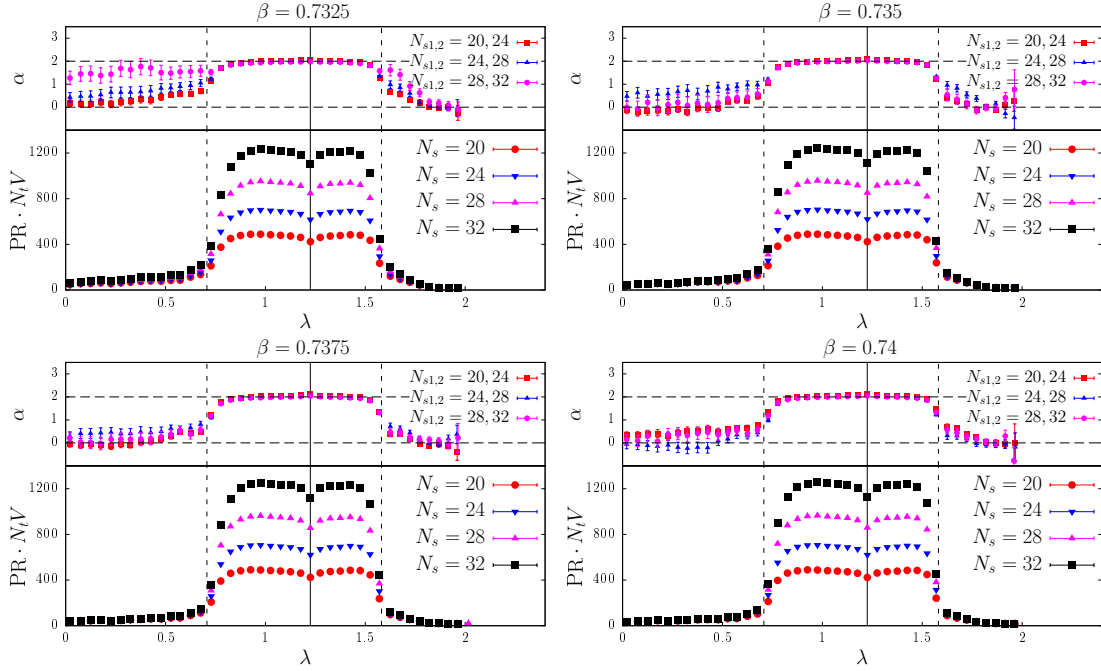


Figure 2: Deconfined phase, physical sector: mode size  $\text{PR} \cdot N_t V = \text{IPR}^{-1}$  and fractal dimension  $\alpha$ .

bulk modes are delocalized in both phases, see Figs. 1–3 (top panels). The low modes, instead, while delocalized in the low-temperature phase, become localized in the high-temperature phase, up to some critical point in the spectrum. More precisely, in the confined phase low modes are delocalized but with a nontrivial fractal dimension, which starting from around  $\alpha \approx 1$  for the lowest modes increases toward 2 as one approaches the bulk. In the deconfined phase, instead, for low modes  $\alpha$  is close to 0, and starts increasing toward 2 at some point  $\lambda_c$ , which we identify as the mobility edge. While difficult to locate with the current precision, the results shown in Figs. 2 and 3 suggest that  $\lambda_c < \lambda_{(0)}$ , up to the largest available value of  $\beta$ , and that it increases with  $\beta$ . Finally, the high modes are localized in both phases, above a second mobility edge  $\lambda'_c$ , identified as the point where  $\alpha$ , after decreasing from its bulk value, reaches again 0. In this case the results in Figs. 1–3 suggest that  $\lambda'_c > \lambda_{(1)}$  up to the largest available value of  $\beta$ . While in the confined phase there seems to be little or no dependence on  $\beta$ ,  $\lambda'_c$  seems to decrease with  $\beta$  in the deconfined phase.

Very large fluctuations in the fractal dimension of the low modes, and of the high modes near  $\lambda_{(1)}$ , are apparent near  $\beta_c$ . These are a consequence of large finite-size effects, originating from the tunnelling of the system between the two phases, where low modes have different localization properties. A similar explanation holds for the high modes right above  $\lambda_{(1)}$ : the second mobility edge,  $\lambda'_c$ , seems in fact independent of  $\beta$  below

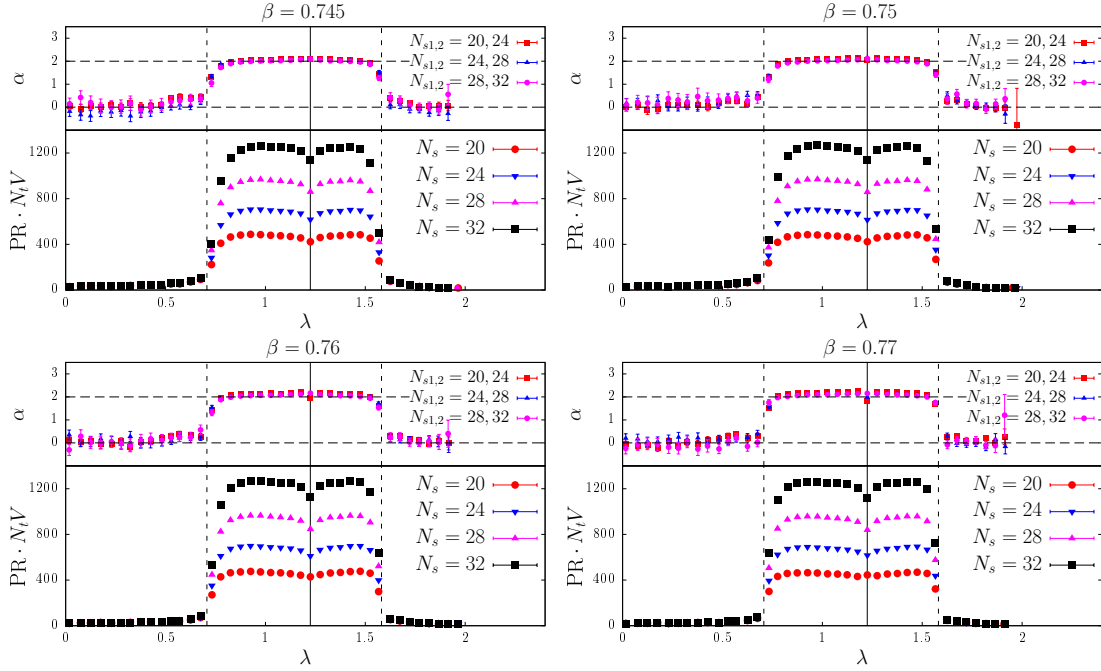


Figure 3: Deconfined phase, physical sector: mode size  $\text{PR} \cdot N_t V = \text{IPR}^{-1}$  and fractal dimension  $\alpha$  (continued).

$\beta_c$  while it decreases with  $\beta$  above  $\beta_c$ , and tunnelling between the two phases leads to contributions from the “wrong” type of modes. The contribution of these tunnelling configurations are however expected to become negligible as the system size is increased.

Notice that the estimate of the fractal dimension of the bulk modes in the deconfined phase, obtained from the available volumes, sometimes exceeds 2. This is clearly a finite-size effect, indicating that the volume scaling of the bulk modes has not yet reached its asymptotic behavior (which must be such that  $\alpha \leq 2$ ). This effect is present, and actually stronger, far away from  $\beta_c$ , and is most likely of a different origin than tunneling configurations. A possible explanation is that, as the system grows, not only the effective support of the bulk modes keeps increasing at the same rate, but at the same time these modes become also more uniformly distributed on their support. In any case, our results indicate that  $\alpha$  keeps approaching 2 (from above) as the lattice volume grows.

As we mentioned above in Section 3, in the deconfined phase of the present model we do not expect an abrupt change from localized ( $\alpha = 0$ ) to fully delocalized ( $\alpha = 2$ ) modes even in the thermodynamic limit. A spectral range with volume-independent non-trivial fractal dimension seems to be present around  $\lambda_{(0)}$ . This is consistent with the BKT nature of the Anderson transition expected for this model. However, a detailed study of this issue, as well as the precise location of the mobility edge, is beyond our reach with the available statistics and system sizes. It seems however beyond doubt that the

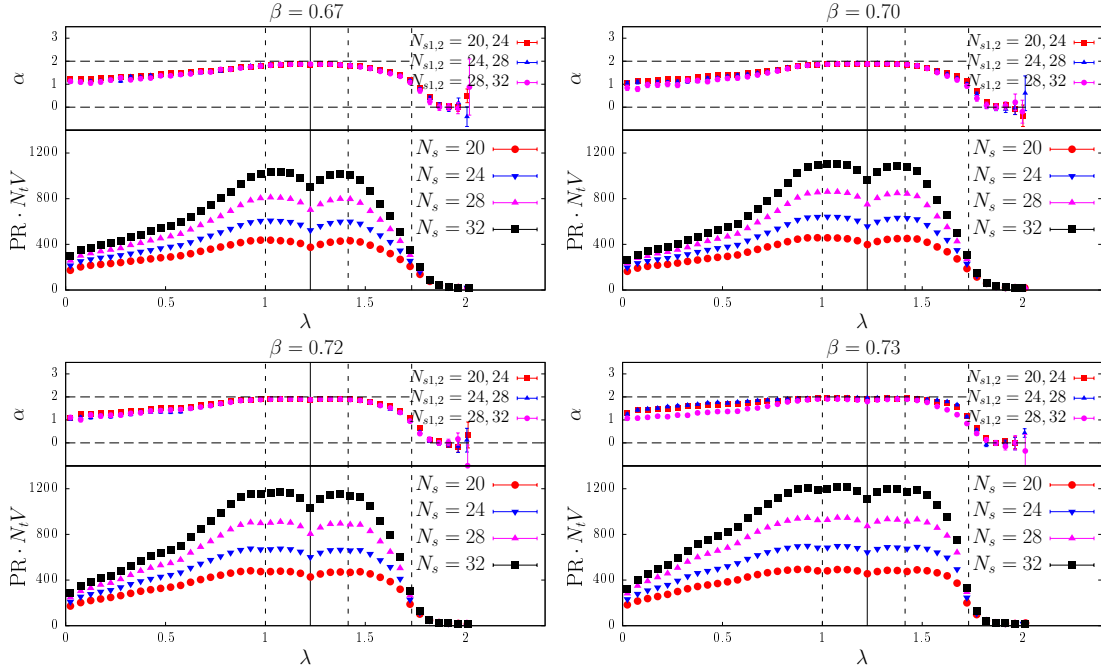


Figure 4: Confined phase, unphysical sector: mode size  $\text{PR} \cdot N_t V = \text{IPR}^{-1}$  and fractal dimension  $\alpha$ . The points  $\lambda_{(1)}^{\text{PBC}}$ ,  $\lambda_*$ ,  $\lambda_{(2)}^{\text{PBC}}$  and  $\lambda_{(3)}^{\text{PBC}}$  (see Eq. (30)) are marked with vertical lines.

localization properties of the low modes change across the transition, and the presence of a mobility edge seems very likely.

The clear separation of low, bulk and high modes at high temperature is not surprising. In fact, as  $\beta$  increases the Polyakov loop becomes more and more ordered, inducing stronger and stronger correlations among time slices. This brings the system to fluctuate more and more closely around the trivial configuration, whose Dirac spectrum lies exactly in the range  $[\lambda_{(0)}, \lambda_{(1)}]$ . It is then not unexpected that modes at both edges of the positive spectrum tend to localize, as they are probably related to the local fluctuations of the gauge configurations away from the trivial one. This will be investigated in detail in Subsection 4.3. It is interesting to note that also the point  $\lambda_*$  is singled out, with a clear dip in the PR; however, we have no explanation for this behavior.

#### 4.1.2 Unphysical sector

The analogue of the trivial configuration in the unphysical sector is the gauge configuration with  $U_{2,3}(n) = 1 \forall n$ ,  $U_1(n) = 1$  if  $n_1 < N_t - 1$ ,  $U_1(n) = -1$  if  $n_1 = N_t - 1$ . The spectrum of the staggered operator on this configuration is equal to that obtained with the trivial configuration but with temporal boundary conditions switched to periodic

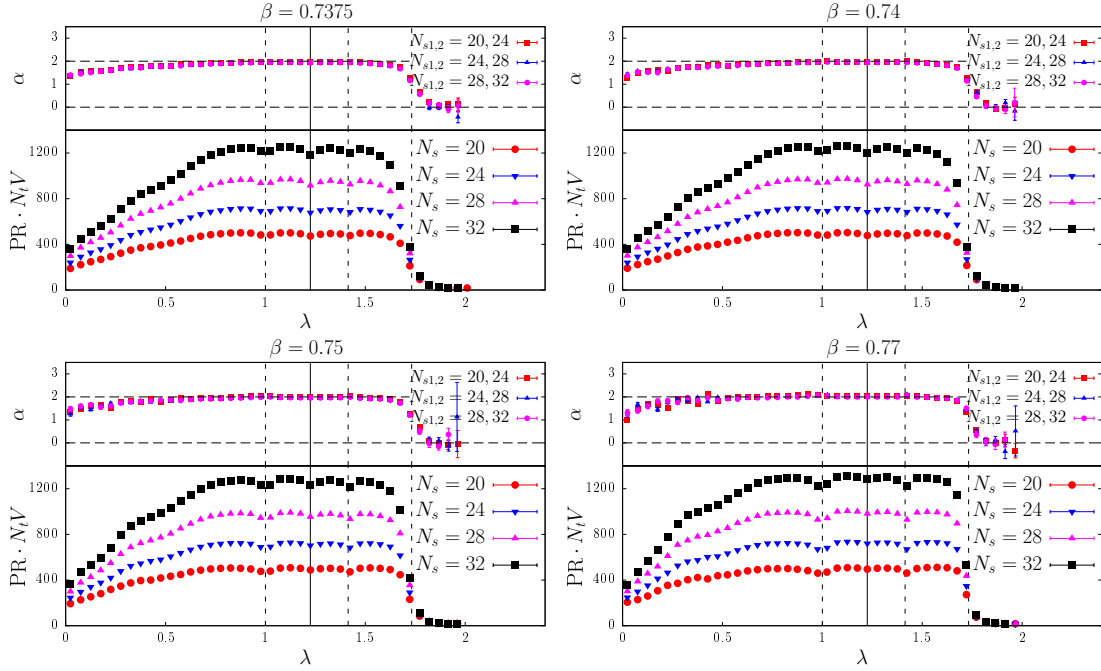


Figure 5: Deconfined phase, unphysical sector: mode size  $\text{PR} \cdot N_t V = \text{IPR}^{-1}$  and fractal dimension  $\alpha$ .

instead of antiperiodic,

$$\lambda_{\text{free}}^{\text{PBC}} = \pm \sqrt{(\sin \omega_k^{\text{PBC}})^2 + (\sin p_1)^2 + (\sin p_2)^2}, \quad (29)$$

where  $p_j$  have been defined under Eq. (27), and  $\omega_k^{\text{PBC}} = \frac{2k\pi}{N_t}$ ,  $k = 0, \dots, N_t - 1$ . For  $N_t = 4$  one has  $(\sin \omega_{0,2}^{\text{PBC}})^2 = 0$ ,  $(\sin \omega_{1,3}^{\text{PBC}})^2 = 1$ . In analogy with the physical sector, one then expects that, at least at high temperature, the points

$$\begin{aligned} \lambda_{(0)}^{\text{PBC}} &\equiv 0, & \lambda_{(1)}^{\text{PBC}} &\equiv \sin \frac{\pi}{2} = 1, \\ \lambda_{(2)}^{\text{PBC}} &\equiv \sqrt{2}, & \lambda_{(3)}^{\text{PBC}} &\equiv \sqrt{(\sin \frac{\pi}{2})^2 + 2} = \sqrt{3}, \end{aligned} \quad (30)$$

that correspond to the boundaries of the Matsubara sectors, are singled out in the spectrum. Indeed, as  $\beta$  increases and the system becomes more ordered, one expects the spectrum to resemble more and more the “free” spectrum of Eq. (29).

As a matter of fact, in the low-temperature phase the unphysical sector does not differ much from the physical one: as shown in Fig. 4 (bottom panels), all modes are extended, except at the very high end ( $\lambda > \lambda_{(3)}^{\text{PBC}}$ ) where they are localized. In contrast with the physical sector, though, this does not change qualitatively as one crosses over into the high-temperature phase. As it can be seen in Fig. 5 (bottom panels), the tendency is

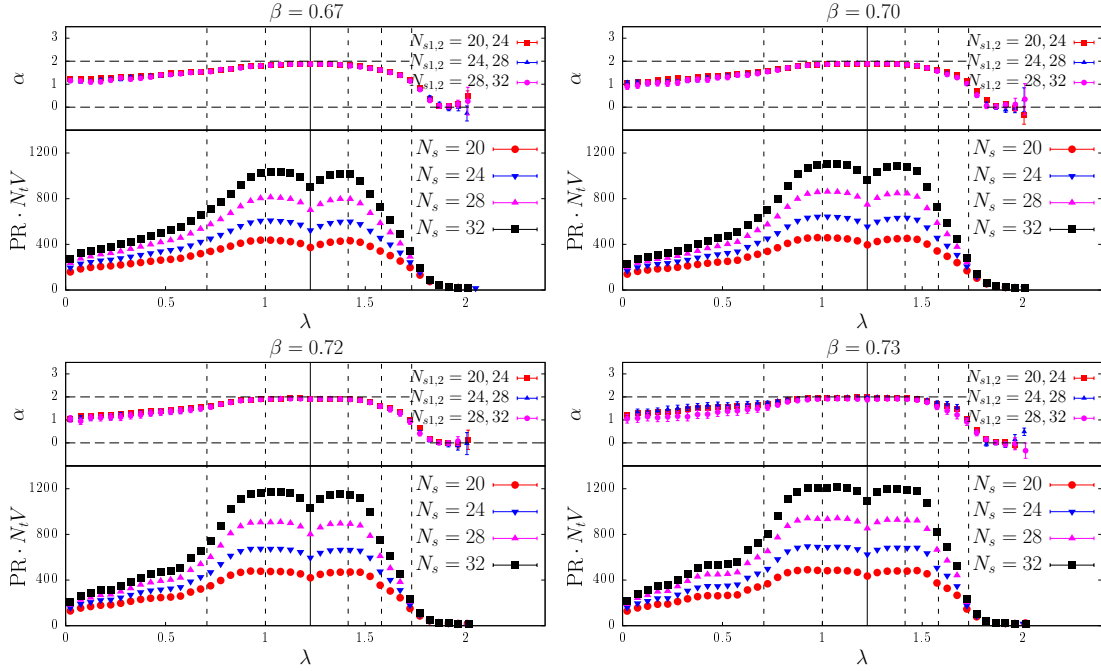


Figure 6: Confined phase, both sectors combined: mode size  $\text{PR} \cdot N_t V = \text{IPR}^{-1}$  and fractal dimension  $\alpha$ . The points  $\lambda_{(0)}$ ,  $\lambda_{(1)}^{\text{PBC}}$ ,  $\lambda_*$ ,  $\lambda_{(2)}^{\text{PBC}}$ ,  $\lambda_{(1)}$  and  $\lambda_{(3)}^{\text{PBC}}$  (see Eqs. (28) and (30)) are marked with vertical lines.

for the mode size to increase everywhere below  $\lambda < \lambda_{(3)}^{\text{PBC}}$  (especially below  $\lambda_{(1)}^{\text{PBC}}$  and above  $\lambda_{(2)}^{\text{PBC}}$ ), and to change very little at the high end  $\lambda > \lambda_{(3)}^{\text{PBC}}$ . Figs. 4 and 5 (bottom panels) suggest that a mobility edge is present at the high end of the spectrum, and that it depends on  $\beta$  very little, or not at all, in both phases of the theory. More detailed information is provided by the fractal dimension, shown in Figs. 4, 5 (top panels). In the confined phase one finds the same situation as in the physical sector, with delocalized low modes with nontrivial fractal dimension  $\alpha \approx 1$ , delocalized bulk modes with  $\alpha \approx 2$ , and localized high modes ( $\alpha = 0$ ) above some  $\lambda'_c$ . While no qualitative change is seen when crossing over into the deconfined phase, quantitatively one observes that both the low and bulk modes tend to become more delocalized, with  $\alpha$  getting closer to 2 as  $\beta$  increases. Not much seems to change for the high modes above  $\lambda_{(3)}^{\text{PBC}}$ , with  $\lambda'_c$  barely moving, if at all. As expected, the points  $\lambda_{(i)}^{\text{PBC}}$  correspond to features in the PR at high  $\beta$ , as does again the point  $\lambda_*$ : specifically, dips are present at  $\lambda_{(1)}^{\text{PBC}}$ ,  $\lambda_{(2)}^{\text{PBC}}$ , and  $\lambda_*$ , and the mode size decreases dramatically above  $\lambda_{(3)}^{\text{PBC}}$ . In contrast with the physical sector, there is no overshooting of the fractal dimension above 2 for the bulk modes, and only near  $\lambda_{(1)}^{\text{PBC}}$  and  $\lambda_{(2)}^{\text{PBC}}$  one can observe a small effect for the largest  $\beta$  values.

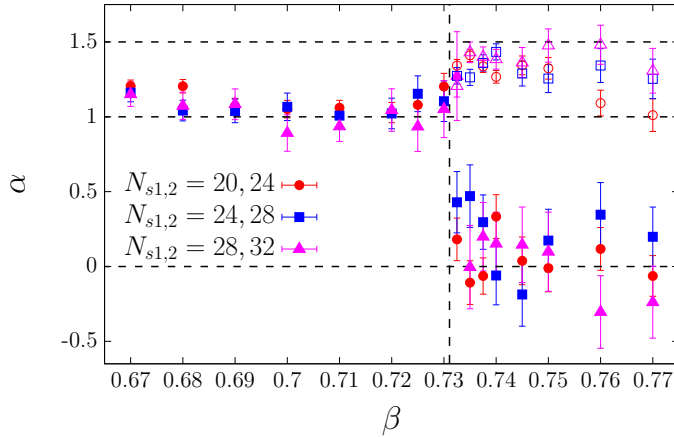


Figure 7: Fractal dimension in the lowest spectral bin, with physical and unphysical sectors combined in the confined phase, and shown separately in the deconfined phase, estimated with various pairs of system sizes. The critical coupling  $\beta_c$  is marked by the dashed vertical line.

#### 4.1.3 Confined phase: both sectors combined

As already pointed out above, in the confined phase both sectors contribute equally to physical observables. We show the resulting mode size and fractal dimension in Fig. 6. Given the similar behavior in the two sectors when  $\beta < \beta_c$ , these plots show little difference from those obtained for the two sectors separately. These plots confirm the presence of localized modes only at the high end of the spectrum, with a mobility edge that shows little to no dependence on  $\beta$ ; and that low modes have a nontrivial fractal dimension.

#### 4.1.4 Near-zero modes

In order to summarize the dependence on temperature of the localization properties of the low modes, in Figs. 7 and 8 we show the fractal dimension of modes in the lowest spectral bin, as a function of  $\beta$ . More precisely, in Fig. 7 we show estimates of the fractal dimension obtained from several pairs of volumes, treating the two center sectors together in the confined phase, and separately in the deconfined phase. For  $\beta < \beta_c$ ,  $\alpha$  tends to slightly decrease as  $\beta$  increases, from slightly above 1 toward 1 up to around  $\beta_c$ . Above  $\beta_c$  it drops toward 0, in the physical sector, and increases to approximately  $1.2 \div 1.4$ , in the unphysical sector. Finite-size effects are small at low  $\beta$ , expectedly large around  $\beta_c$ , and again reasonably small above  $\beta_c$ , although larger than in the low-temperature phase. In Fig. 8 we show an estimate of the fractal dimension  $\alpha$  of the lowest modes obtained after averaging over all pairs of available system sizes. Error bars correspond to the sum in quadrature of the average statistical error and of the finite-size systematic error,

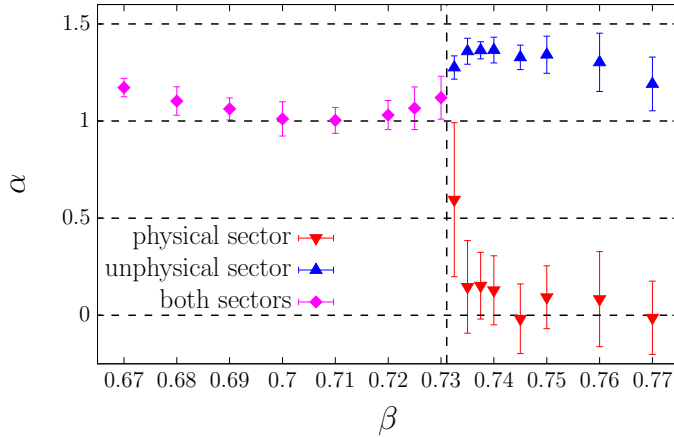


Figure 8: Fractal dimension in the lowest spectral bin, estimated by averaging over all pairs of system sizes with  $20 \leq N_s \leq 32$ . The two center sectors are combined for  $\beta < \beta_c$ , and shown separately for  $\beta > \beta_c$ , with  $\beta_c$  marked by the dashed vertical line.

estimated as the variance of  $\alpha$  over the pairs of  $N_s$  values. Our results show clearly that the two center sectors respond very differently to the phase transition, with low modes becoming more delocalized in the unphysical sector, and localized in the physical sector.

Although the use of only moderately large volumes, for which large finite-size effects are still present near  $\beta_c$ , does not allow us to make a conclusive statement, it seems likely that in the thermodynamic limit an abrupt transition from  $\alpha \approx 1$  to  $\alpha = 0$  will take place at  $\beta_c$  in the physical sector. Conclusive evidence requires the extension of the present study to larger system sizes.

## 4.2 Spectral density

The spectral density per unit lattice volume,  $\rho$ ,

$$\rho(\lambda) \equiv (N_t V)^{-1} \langle \sum_l \delta(\lambda - \lambda_l) \rangle, \quad (31)$$

is shown in Fig. 9 for several values of  $\beta$ , for the physical and unphysical sectors separately, and for both sectors together in the confined phase. The dependence on the system size is negligible, so only the largest size  $N_s = 32$  is shown. The points  $\lambda_{(i)}$ ,  $i = 0, 1, 2$  and  $\lambda_{(i)}^{\text{PBC}}$ ,  $i = 1, 2, 3$ , as well as  $\lambda_*$ , are marked. The spectral density is large in the bulk and small at the low and high ends; remarkably, it does not vanish at the low end  $\lambda \simeq 0$  in either phase. The spectral density  $\rho(0^+)$  in the lowest bin  $[0, \Delta\lambda]$  is shown in Fig. 10, again for  $N_s = 32$ , for the two center sectors separately and for both sectors combined (also in the deconfined phase for comparison). While  $\rho(0^+)$  keeps decreasing with  $\beta$ , it remains nonzero in both sectors up to the largest  $\beta$  studied here. Loosely speaking, this indicates chiral symmetry breaking by a (valence) quark-antiquark condensate both in the confined and in the deconfined phase of the theory.

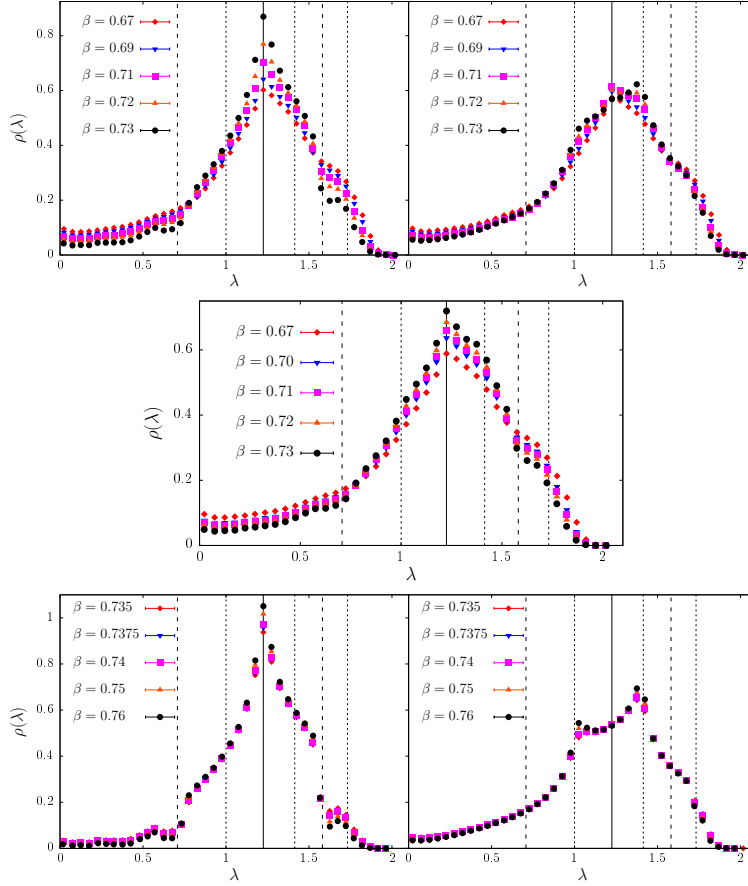


Figure 9: Spectral density – confined phase, physical (top left) and unphysical (top right) sector, and both sectors together (center); deconfined phase, physical (bottom left) and unphysical (bottom right) sector. The points  $\lambda_{(0)}$ ,  $\lambda_{(1)}^{\text{PBC}}$ ,  $\lambda_*$ ,  $\lambda_{(2)}^{\text{PBC}}$ ,  $\lambda_{(1)}$  and  $\lambda_{(3)}^{\text{PBC}}$  (see Eqs. (28) and (30)) are marked with vertical lines. Here  $N_s = 32$ .

Furthermore, comparing the physically meaningful results, i.e., both sectors added up in the confined phase and treated separately in the deconfined phase, one sees that  $\rho(0^+)$  jumps at  $\beta_c$ , downwards (resp. upwards) if the physical (resp. unphysical) sector is chosen in the deconfined phase. Notice that since the spectral density near zero is smaller (resp. larger) in the physical (resp. unphysical) sector, this sector will be favored in the presence of dynamical fermions (resp. pseudofermions), as anticipated (see Ref. 3). This means, again in a loose sense, that chiral symmetry remains broken in the high- $\beta$  phase but a first-order phase transition is displayed in the chiral properties. Moreover, in the physical sector in the deconfined phase the low modes are localized.

A similar situation is found in SU(3) pure-gauge theory in 3+1 dimensions, where however the near-zero localized modes stand out as a prominent peak [18, 20], rather

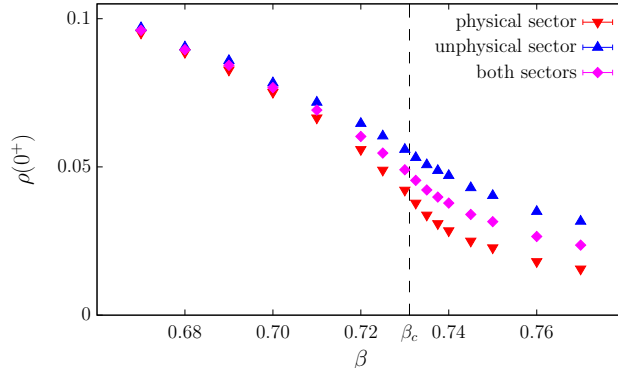


Figure 10: Spectral density of near-zero modes. The case of the two center sectors combined in the deconfined phase is shown only for comparison. Here  $N_s = 32$ .

than being part of a plateau as in the present case.<sup>8</sup> The inclusion of dynamical fermions is expected to lower the density of near-zero modes, but it is possible that even in this case the  $\mathbb{Z}_2$  theory displays a first-order transition to a phase with a non-zero density of localized near-zero modes. If this scenario survived also in the chiral limit (taken after the continuum limit, also assumed to exist), it would lead to the disappearance of the massless Goldstone excitations associated with the spontaneous breaking of the  $SU(N_f = 4)_A$  symmetry of the theory at finite temperature [62]. The connection between localization and disappearance of Goldstone modes was originally made in Ref. [63], in the context of Anderson models, and later rediscovered in Ref. [64], in the context of lattice field theories at zero temperature.

A curious feature is the presence of a peak at  $\lambda_*$  at all  $\beta$  in the physical sector, and at low  $\beta < \beta_c$  in the unphysical sector. At high  $\beta > \beta_c$  in the unphysical sector this peak disappears, and is replaced by two peaks near  $\lambda_{(1)}^{(\text{PBC})}$  and  $\lambda_{(2)}^{(\text{PBC})}$ . We do not know the reason behind these peaks and the analogous presence of features at  $\lambda_*$  (as well as at  $\lambda_{(i)}$  or  $\lambda_{(i)}^{(\text{PBC})}$ ) in most observables considered in this work.

### 4.3 Correlation of localized modes with gauge observables

#### 4.3.1 Polyakov loop

According to the sea/islands picture of localization [16, 23, 24], localized modes in the physical sector of the deconfined phase are expected to live near fluctuations of the

<sup>8</sup>Localization is understood here in the sense of the usual fractal dimension  $\alpha$  (see Eq. (12)) being equal to zero. For a 3+1 dimensional theory this is obtained as follows from the scaling of the PR,  $\text{PR}(\lambda, N_s) \simeq c(\lambda)N_s^{\alpha(\lambda)-3}$ . However, using a different definition  $d_{\text{IR}}$  of fractal dimension, the authors of Ref. [61] find for 3+1 dimensional  $SU(3)$  pure gauge theory that  $d_{\text{IR}} = 2$  for near-zero modes, differing both from  $d_{\text{IR}} = 3$  found for exact zero modes and from  $d_{\text{IR}} = 1$  found for low modes above the peak. The relation between the two definitions of fractal dimensions is not clear yet.

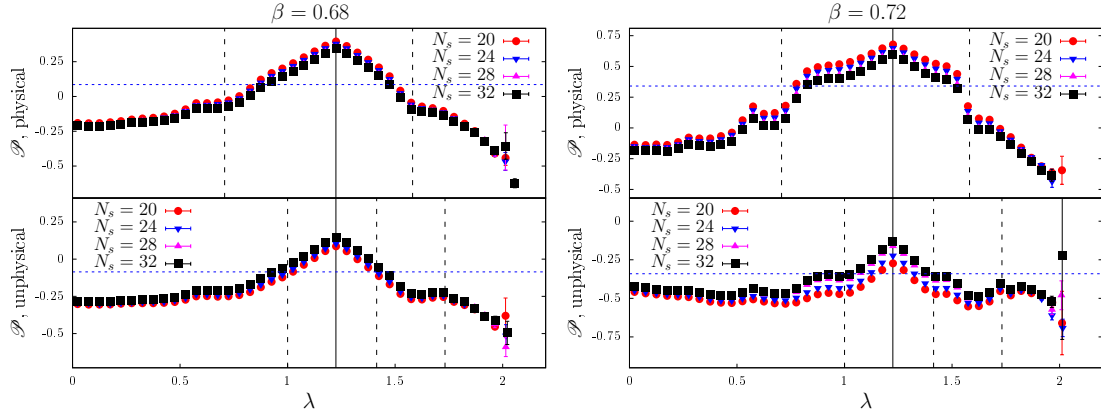


Figure 11: Confined phase: Polyakov loop weighted by the modes. Here and in the following plots, the physical (resp. unphysical) sector is shown in the top (resp. bottom) panel. Horizontal lines correspond to  $\pm\langle|\bar{P}|\rangle$  on the largest available volume ( $N_s = 32$ ).

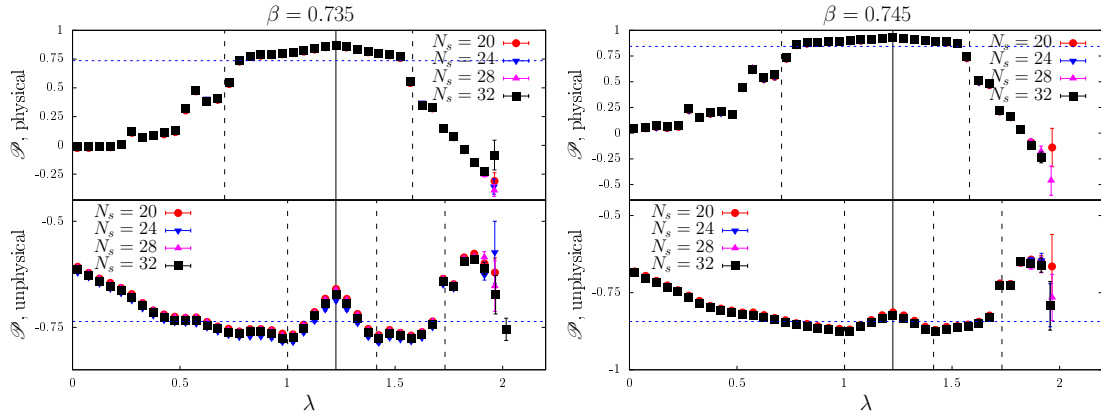


Figure 12: Deconfined phase: Polyakov loop weighted by the modes.

Polyakov loops away from the ordered value. For  $\mathbb{Z}_2$  the Polyakov loop can take only two values, and we expect the localized modes to prefer sites where  $P(\vec{x}) = -1$ . In Figs. 11 and 12 we show the Polyakov loop weighted by the eigenmodes  $\mathcal{P}(\lambda)$ , Eq. (15), for the physical (top panels) and unphysical (bottom panels) sectors. This is compared to the average of  $\bar{P}$  in the respective sectors. By construction, these sector averages are simply  $\pm\langle|\bar{P}|\rangle$ , where the average is over the ensemble of configurations generated in the Monte-Carlo simulation.

Let us discuss first the physical sector. In the confined phase, while delocalized, the low modes show a moderate but clear preference for negative Polyakov loops; the bulk modes show a moderate but clear preference for positive Polyakov loops, with  $\mathcal{P}$  above the average of  $\bar{P}$  in the physical sector; and the high modes, which are localized,

show a clear preference for negative Polyakov loops. Throughout the spectrum,  $\mathcal{P}(\lambda)$  decreases slightly with the volume, probably reflecting the fact that  $\langle |\bar{P}| \rangle \rightarrow 0$  in the thermodynamic limit; it seems likely though that a nontrivial  $\mathcal{P}(\lambda)$  will be found also in this limit. In the deconfined phase the low modes, which are now localized, have roughly half of their weight on sites with positive Polyakov loop and half on the now much rarer sites with negative Polyakov loop. This is in agreement with expectations. More precisely, the ratio between the average fraction of sites with negative Polyakov loop among those “occupied” by a mode and the average fraction of sites with negative Polyakov loop on the whole lattice, i.e.,  $(1 - \mathcal{P}(\lambda))/(1 - \langle |\bar{P}| \rangle)$ , increases steadily with  $\beta$  in the deconfined phase. Bulk modes tend instead to avoid negative Polyakov loops, as shown by the fact that  $1 - \mathcal{P}(\lambda) < 1 - \langle |\bar{P}| \rangle$ . High modes are again clearly preferring negative Polyakov loops, with more than half of the mode’s weight concentrated on the corresponding sites. In the deconfined phase the dependence of  $\mathcal{P}$  on the volume seems very mild.

We now discuss the unphysical sector. In the confined phase, negative Polyakov loops seem again to be preferred everywhere in the spectrum except in the very middle, where positive Polyakov loops are slightly preferred. In fact, also in this case  $\mathcal{P}(\lambda)$  for the bulk modes is above the average of  $\bar{P}$  in the given center sector, although in this case it means that they favor the slightly less frequent positive loops to the negative ones (in the physical sector they prefer instead the more frequent positive loops). Low and high modes instead have  $\mathcal{P}(\lambda) < -\langle |\bar{P}| \rangle$ . The tendency is this time for  $\mathcal{P}(\lambda)$  to increase as the volume increases. In the deconfined phase  $\mathcal{P}(\lambda)$  becomes flatter in the bulk, where  $\mathcal{P}(\lambda)$  gets closer to  $-\langle |\bar{P}| \rangle$ , while low and high modes show now clearly  $0 > \mathcal{P}(\lambda) > -\langle |\bar{P}| \rangle$ , thus favoring positive Polyakov loops; the volume dependence is again very mild. The correlation of low modes with positive Polyakov loops in the deconfined phase cannot be simply explained in terms of “energetically” favorable islands “attracting” the mode. It is, however, not in contrast with the sea/islands picture of localization. We elaborate on this point in the conclusions.

### 4.3.2 Negative plaquettes

We now turn to the correlation between localized modes and negative plaquettes, for which we provide two different measures. In Figs. 13 and 14 we show  $\mathcal{U}(\lambda)$ , which measures the average number of negative plaquettes touched by the modes (see Eq. (17)) or, equivalently, the “negative plaquettes seen by the modes”. In Figs. 15 and 16 we show instead  $\tilde{\mathcal{U}}(\lambda)$ , which measures what fraction of the modes lives on sites touched by at least one negative plaquette (see Eq. (18)). The two observables provide slightly different information:  $\tilde{\mathcal{U}}(\lambda)$  tells us “how much” of the modes is found near negative plaquettes, while  $\mathcal{U}(\lambda)$  tells us how much the modes like to live near *clusters* of negative plaquettes.

We discuss  $\mathcal{U}(\lambda)$  first. In the physical sector (Figs. 13 and 14, top panels) the low and high modes prefer to be closer to negative plaquettes ( $\mathcal{U}(\lambda) > 6\langle 1 - U_{\mu\nu} \rangle$ ), while

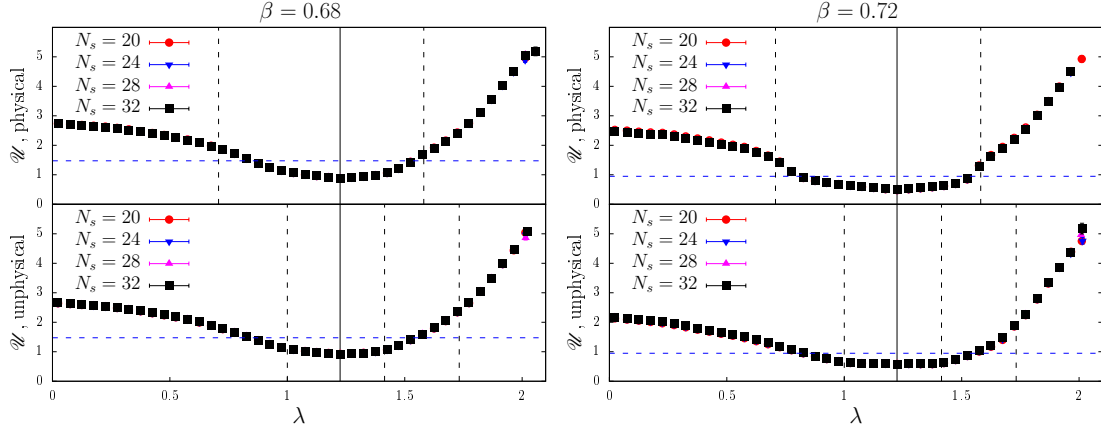


Figure 13: Confined phase: average number of negative plaquettes touched by a mode. Here and in the following plot, horizontal lines correspond to  $6\langle 1 - U_{\mu\nu} \rangle$  on the largest available volume ( $N_s = 32$ ).

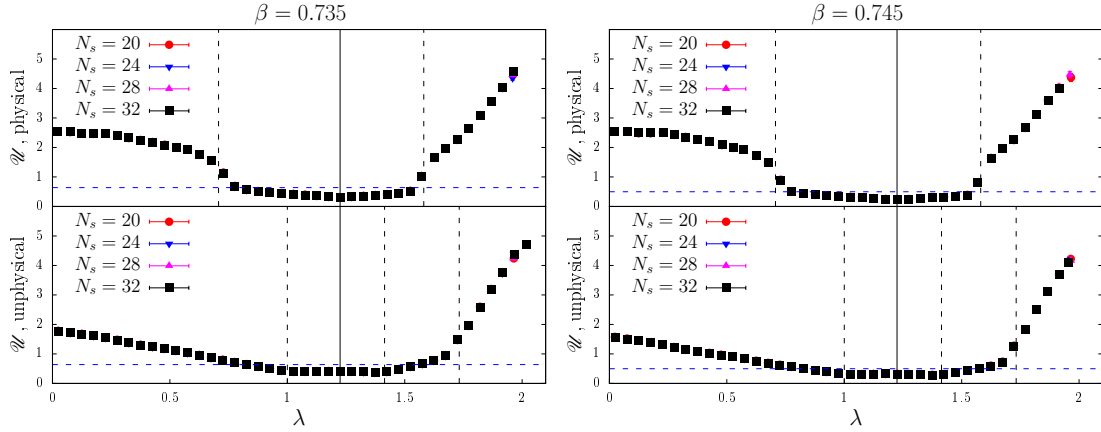


Figure 14: Deconfined phase: average number of negative plaquettes touched by a mode.

bulk modes prefer to avoid them ( $\mathcal{U}(\lambda) < 6\langle 1 - U_{\mu\nu} \rangle$ ), in both phases of the theory. More precisely, the low and, especially, the high modes have a larger weight on sites touching more than one negative plaquette, and so prefer to live close to where negative plaquettes tend to cluster. No clear dependence on the volume is visible.  $\mathcal{U}(\lambda)$  shows little dependence on  $\beta$  as well, the only notable features being that for bulk modes the tendency to avoid negative plaquettes is much less pronounced in the deconfined phase, where  $\mathcal{U}(\lambda)$  also becomes flatter. For the high modes  $\mathcal{U}(\lambda)$  changes very little with  $\beta$ ; for the low modes it slightly decreases as the deconfined phase is approached, remaining essentially constant in the deconfined phase. Since the average number of negative plaquettes decreases as  $\beta$  is increased, this means that the localized low and

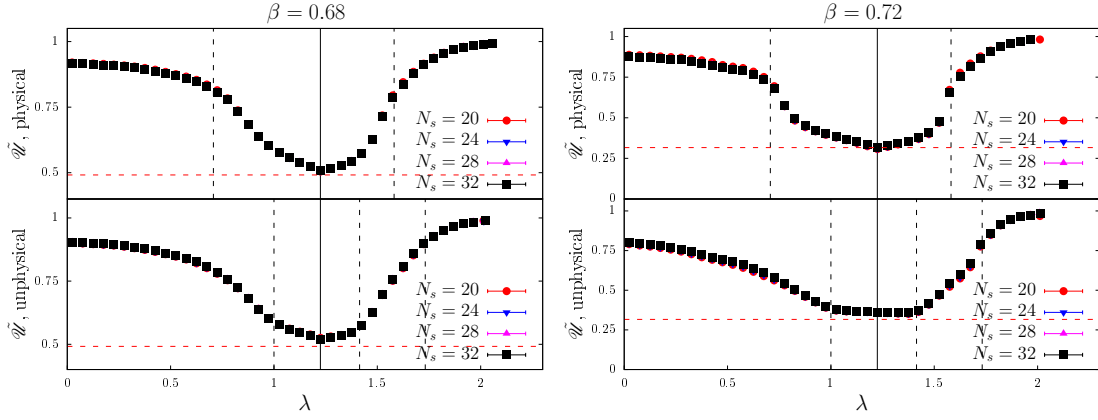


Figure 15: Confined phase: fraction of mode touched by negative plaquettes. Here and in the following plot, horizontal lines correspond to  $2(1 - \langle U_{\mu\nu} \rangle)$  on the largest available volume ( $N_s = 32$ ).

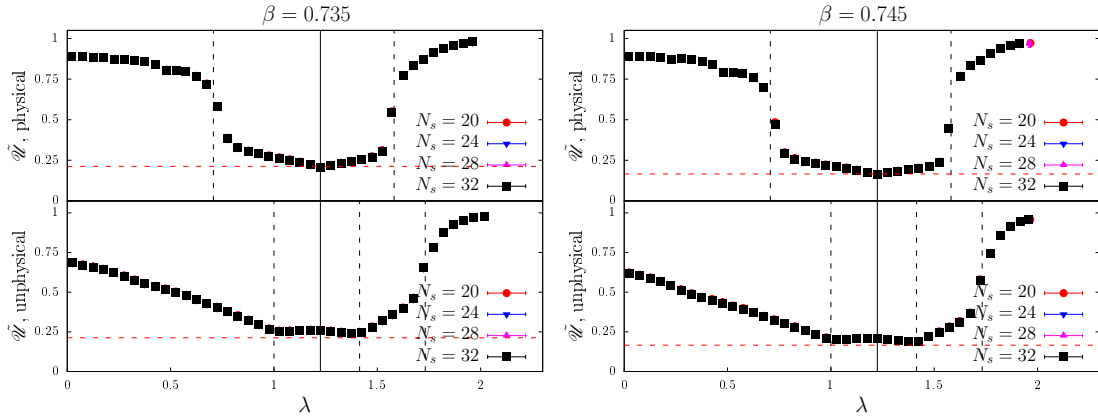


Figure 16: Deconfined phase: fraction of mode touched by negative plaquettes.

high modes are more and more localized near clusters of negative plaquettes as one gets deeper in the deconfined phase.

The situation is quite similar in the unphysical sector (Figs. 13 and 14, bottom panels): low and high modes still prefer to be near clusters of negative plaquettes, and bulk modes prefer to avoid them. Again, no clear volume dependence is visible. The dependence on  $\beta$  is slightly stronger than in the physical sector: here not only  $\mathcal{U}(\lambda)$  for bulk modes becomes flatter and closer to  $6(1 - U_{\mu\nu})$  as  $\beta$  increases, but also the upward deviation of  $\mathcal{U}(\lambda)$  from  $6(1 - U_{\mu\nu})$  for low modes becomes less pronounced. As low and bulk modes are delocalized, this is in line with the fact that negative plaquettes become less frequent in the deconfined phase. For the localized high modes the change of  $\mathcal{U}(\lambda)$  with  $\beta$  is small, indicating again that they prefer to localize more near negative

plaquettes as  $\beta$  increases.

We now turn to  $\tilde{\mathcal{W}}(\lambda)$ . In the physical sector (Figs. 15 and 16, top panels), and for all  $\beta$ , 80% or more of the weight of low and high modes is on sites touching at least one negative plaquette, while for bulk modes this fraction is 80% or less, and decreasing rapidly as one approaches  $\lambda_*$  from either side. For low and high modes there seems to be little variation as  $\beta$  increases, despite the fact that negative plaquettes become rarer, while for bulk modes  $\tilde{\mathcal{W}}(\lambda)$  clearly decreases with  $\beta$ . This again indicates that localized modes tend to localize near negative plaquettes. In the unphysical sector (Figs. 15 and 16, bottom panels), low and high modes have again a much larger value of  $\tilde{\mathcal{W}}(\lambda)$  than bulk modes at all  $\beta$ s. Differently from the physical sector,  $\tilde{\mathcal{W}}(\lambda)$  clearly decreases as  $\beta$  increases both for low and bulk modes, while for high modes it shows very little dependence on  $\beta$ . This again indicates that the localized high modes prefer to localize near negative plaquettes. As already mentioned in Section 3, it is not straightforward to estimate what one should expect for  $\tilde{\mathcal{W}}(\lambda)$  in the case of fully delocalized modes ( $|\psi|^2 \sim 1/(N_t V)$ ). It turns out that  $2(1 - \langle U_{\mu\nu} \rangle)$  provides an accurate lower bound on  $\tilde{\mathcal{W}}(\lambda)$  in the bulk of the spectrum.

The stronger correlation between localized modes and negative plaquettes than between localized modes and Polyakov loop fluctuations does not necessarily mean that the former are better candidates as the relevant source of disorder than the latter. On the one hand, negative plaquettes are strongly correlated with Polyakov loop fluctuations. On the other hand, localized modes in the deconfined phase, physical sector, are not strictly confined to Polyakov loop fluctuations away from the ordered value, as that would be “energetically” expensive. One can then reconcile the observed stronger correlation with negative plaquettes and the Polyakov loop fluctuations being the actual source of disorder, if localization takes place on clusters of negative plaquettes near the Polyakov loop fluctuations. This is particularly interesting in the light of the observation [58] that the largest negative-plaquette cluster scales as the system size in the confined phase, while it remains finite in the deconfined phase. This may help explain the relation between deconfinement and localization (and between confinement and delocalization) of the low modes in the physical sector. This point deserves a more detailed study, which is however outside of the scope of the present paper.

#### 4.4 Inertia tensor of the eigenmodes

The inertia tensor of the eigenmodes is expected not only to distinguish between localized and delocalized modes, but also to provide more detailed information on their shape. This requires that a general model for the shape of the eigenmodes is given first, so that the principal axes of the mode,  $v_{1,2,3}$ , and the associated principal moments of inertia,  $\theta_1 \geq \theta_2 \geq \theta_3$ , can be directly related to geometric features. What specific model is used to describe the geometry of the mode is, however, not so important, since we are mostly after generic features such as the scaling of the mode with the lattice size, and, for localized modes, whether they are isotropic or not.

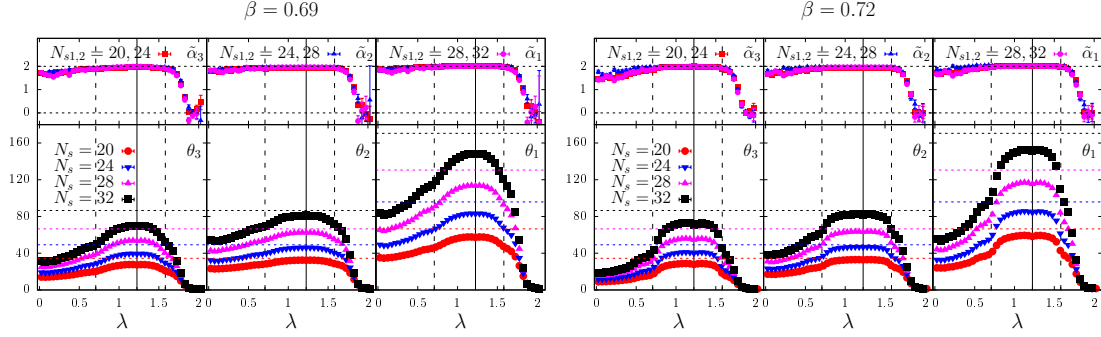


Figure 17: Confined phase, physical sector. Bottom panels: average principal moments of inertia  $\theta_i$ . Here and in the following plots, the expectation for a cuboid of size  $N_t \times N_s \times N_s$  is also shown (color code matching that of the numerical data for the various volumes). Top panels: scaling dimension  $\tilde{\alpha}_i$  of moment  $\theta_i$  for various pairs of volumes.

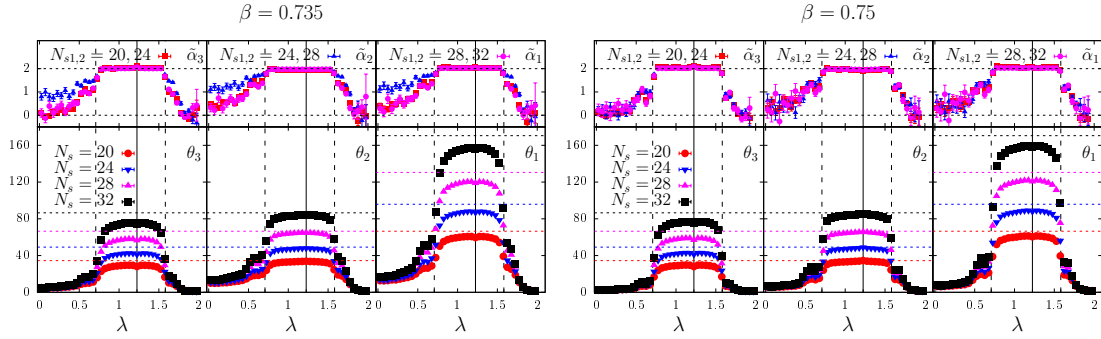


Figure 18: Deconfined phase, physical sector. Bottom panels: average principal moments of inertia  $\theta_i$ . Top panels: scaling dimension  $\tilde{\alpha}_i$  of moment  $\theta_i$  for various pairs of volumes.

For delocalized modes the natural model is a cuboid of unit mass and uniform density extending throughout the whole lattice. For a cuboid of linear size  $\ell_i$  in direction  $v_i$ , one finds for the principal moment of inertia  $\theta_1$  corresponding to the principal axis  $v_1$  the value  $\theta_1^{\text{cont}} = \frac{1}{12}(\ell_2^2 + \ell_3^2)$  for a continuous mass distribution, and  $\theta_1^{\text{lat}} = \frac{1}{12}(\ell_2^2 + \ell_3^2 - 2)$  on a periodic lattice; similar expressions hold for the other two principal moments  $\theta_{2,3}$  corresponding to the principal axes  $v_{2,3}$ . Localized modes can also be modelled as cuboids, this time confined to a limited spatial region, or perhaps more naturally as ellipsoids of extension  $\ell'_i$  in direction  $v_i$ . In the latter case one finds  $\theta_1^{\text{cont}} = \frac{1}{20}(\ell_2^2 + \ell_3^2)$  (for a continuous mass distribution), and similar expressions for the other moments.

For either model, the localized or delocalized nature of the modes should be reflected in the scaling of the moments of inertia with the spatial size  $N_s$  of the lattice,  $\theta_i \sim N_s^{\tilde{\alpha}_i}$ . In fact, using either a cuboid or an ellipsoid model, for a spatially delocalized mode at least one of the two contributions to any of the principal moments should scale like  $N_s^2$ ,

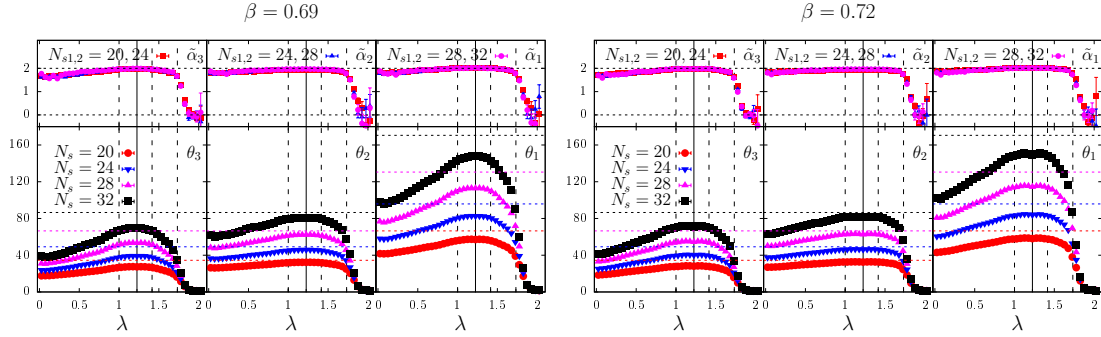


Figure 19: Confined phase, unphysical sector. Bottom panels: average principal moments of inertia  $\theta_i$ . Top panels: scaling dimension  $\tilde{\alpha}_i$  of moment  $\theta_i$  for various pairs of volumes.

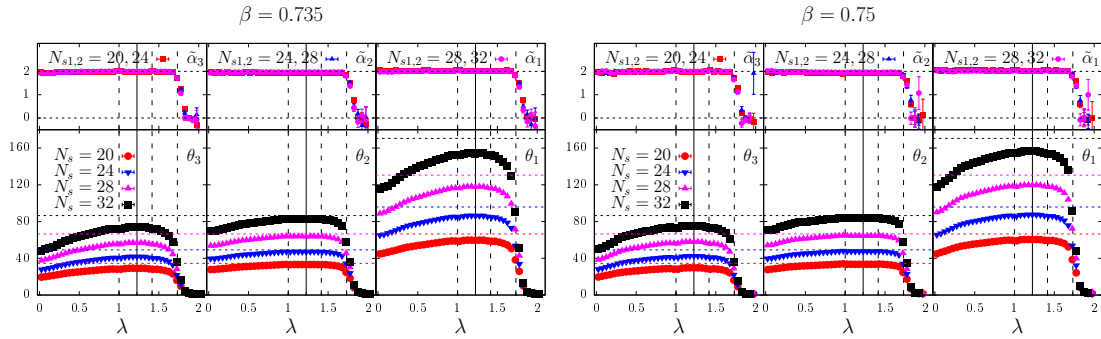


Figure 20: Deconfined phase, unphysical sector. Bottom panels: average principal moments of inertia  $\theta_i$ . Top panels: scaling dimension  $\tilde{\alpha}_i$  of moment  $\theta_i$  for various pairs of volumes.

resulting in  $\tilde{\alpha}_i = 2$ . For localized modes, instead, all the contributions should remain finite as  $N_s$  grows, resulting in  $\tilde{\alpha}_i = 0$ .

Information about how the modes are stretched or flattened in the various directions can be obtained from  $\theta_i$ . The isotropy, or sphericity, of the mode, can be measured by  $\frac{1}{2} \log \frac{\theta_1}{\theta_3}$ : the closer to zero, the closer the mode is to isotropic/spherical ( $\theta_1 \approx \theta_2 \approx \theta_3$ ). The prolateness or oblateness of a mode can be measured instead by  $\log \frac{\theta_2}{\theta_3} - \frac{1}{2} \log \frac{\theta_1}{\theta_3} = \frac{1}{2} \log \frac{\theta_2^2}{\theta_1 \theta_3}$ . Indeed, for a “rod-like” cuboid or a prolate spheroid ( $\theta_1 \approx \theta_2 > \theta_3$ ) this quantity is positive, and the larger in magnitude the more elongated the mode is. Instead, for a “slab-like” cuboid or an oblate spheroid ( $\theta_1 > \theta_2 \approx \theta_3$ ) this quantity is negative, and the larger in magnitude the more flattened the mode is.

Finally, from the principal axes one can determine the typical orientation of the eigenmodes with respect to the temporal direction. For delocalized modes extended throughout the lattice, one expects  $v_1$  to lie along the temporal direction, and  $v_{2,3}$  to lie in the spatial plane. For localized modes one can further distinguish between modes

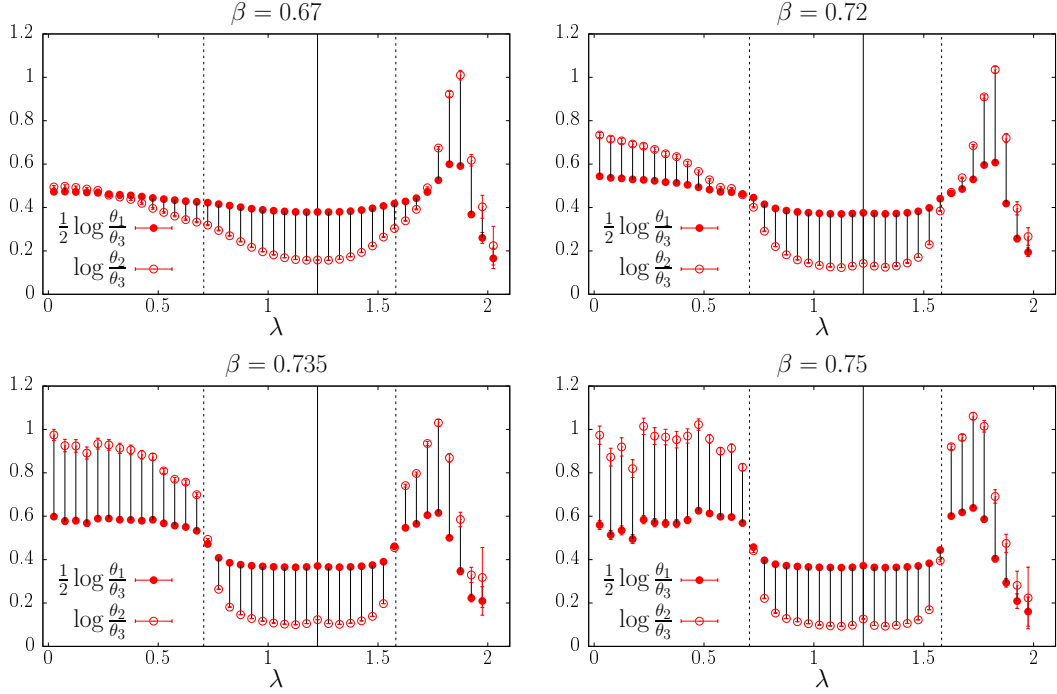


Figure 21: Confined (top row) and deconfined (bottom row) phase, physical sector: shape of the eigenmodes. Here and in the next plot, the quantity  $\frac{1}{2} \log \frac{\theta_1}{\theta_3}$  measures the sphericity, and the difference  $\log \frac{\theta_2}{\theta_3} - \frac{1}{2} \log \frac{\theta_1}{\theta_3} = \frac{1}{2} \log \frac{\theta_2^2}{\theta_1 \theta_3}$  measures the prolateness (if  $> 0$ ) or oblateness (if  $< 0$ ) of the modes. The system size is fixed to  $N_s = 32$ .

extended in the temporal direction, and modes localized in the temporal direction (possibly on a comparable scale). In the first case one similarly expects one principal axis along the temporal direction and two in the spatial plane, while in the second case the orientation of the mode with respect to the temporal direction can fluctuate.

We now discuss our numerical results, separating physical and unphysical sector, and looking at how the modes change across the transition.

**Moments of inertia** In Figs. 17–20, bottom panels, we show the average principal moments of inertia  $\theta_i$  of the eigenmodes, computed locally in the spectrum, for various  $\beta$  and spatial sizes  $N_s$ . For comparison, we also show the theoretical expectation for a uniform  $N_t \times N_s \times N_s$  cuboid extended throughout the lattice. In the top panels we show the corresponding scaling dimension  $\tilde{\alpha}_i$ .

In the physical sector in the confined phase, Fig. 17, the low modes clearly differ from the theoretical prediction for a fully delocalized cuboid. However, all  $\tilde{\alpha}_i$  being close to 2 clearly shows that they are delocalized. Modes in the bulk are closer to the theoretical prediction, and correspondingly the  $\tilde{\alpha}_i$  are much closer to 2. The deviations from the

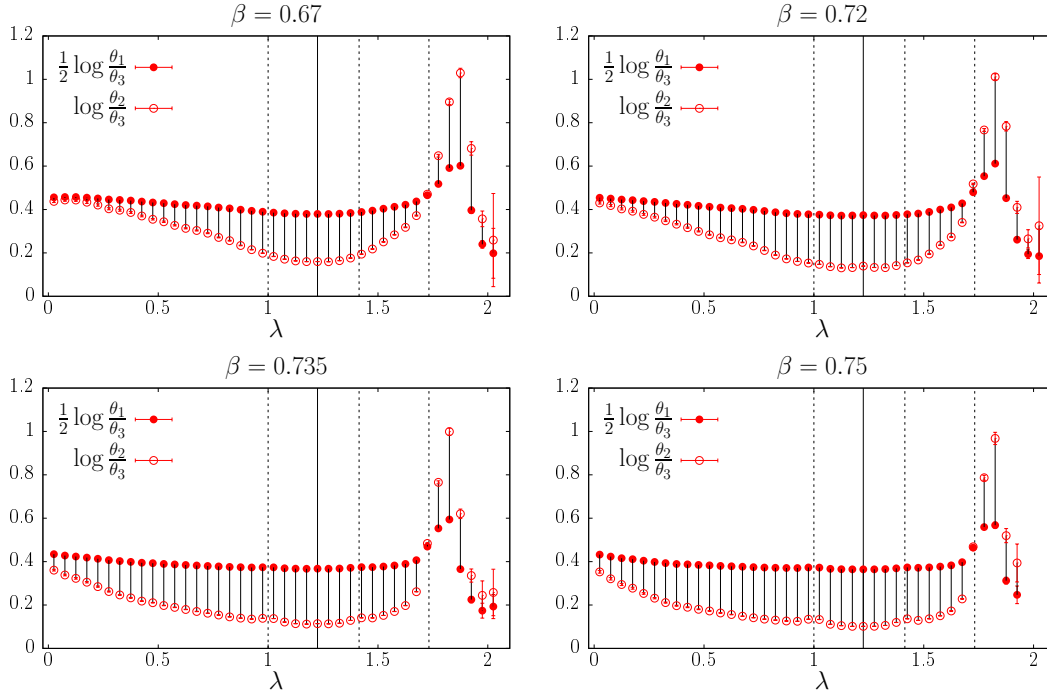


Figure 22: Confined (top row) and deconfined (bottom row) phase, unphysical sector: shape of the eigenmodes.

theoretical expectation clearly visible in  $\theta_1$  and  $\theta_3$  probably reflect the inhomogeneities in the modes due to the tendency to prefer positive Polyakov loops (see Figs. 11 and 12) and avoid negative plaquettes (see Figs. 13 and 14). For high modes, on the other hand, the  $\theta_i$  are independent of  $N_s$ , and correspondingly  $\tilde{\alpha}_i \approx 0$ , consistently with their localized nature. Notice that as  $\beta$  increases, the difference between low and bulk modes becomes sharper, somehow indicating that a phase transition is approaching.

Still in the physical sector but in the deconfined phase, Fig. 18, the moments of inertia of the low modes are now  $N_s$ -independent, indicating that they have become localized. This is confirmed by  $\tilde{\alpha}_i$  becoming approximately 0 above the critical temperature. Notice that sizeable finite-size effects are visible in  $\tilde{\alpha}_i$  close to  $\beta_c$ . For bulk and high modes the moments of inertia and their volume scaling remain approximately the same as in the confined phase.

In the unphysical sector, both in the confined (Fig. 19) and in the deconfined phase (Fig. 20), the moments of inertia show that low and bulk modes are delocalized, with the bulk modes very close to a fully delocalized cuboid, and low modes clearly deviating from it. For high modes the moments of inertia are instead  $N_s$ -independent, consistently with localization, in both phases. Correspondingly,  $\tilde{\alpha}_i \approx 2$  for bulk modes, and  $\tilde{\alpha}_i \approx 0$  for high modes, in both phases. For low modes  $\tilde{\alpha}_i \approx 2$  in the deconfined phase, while

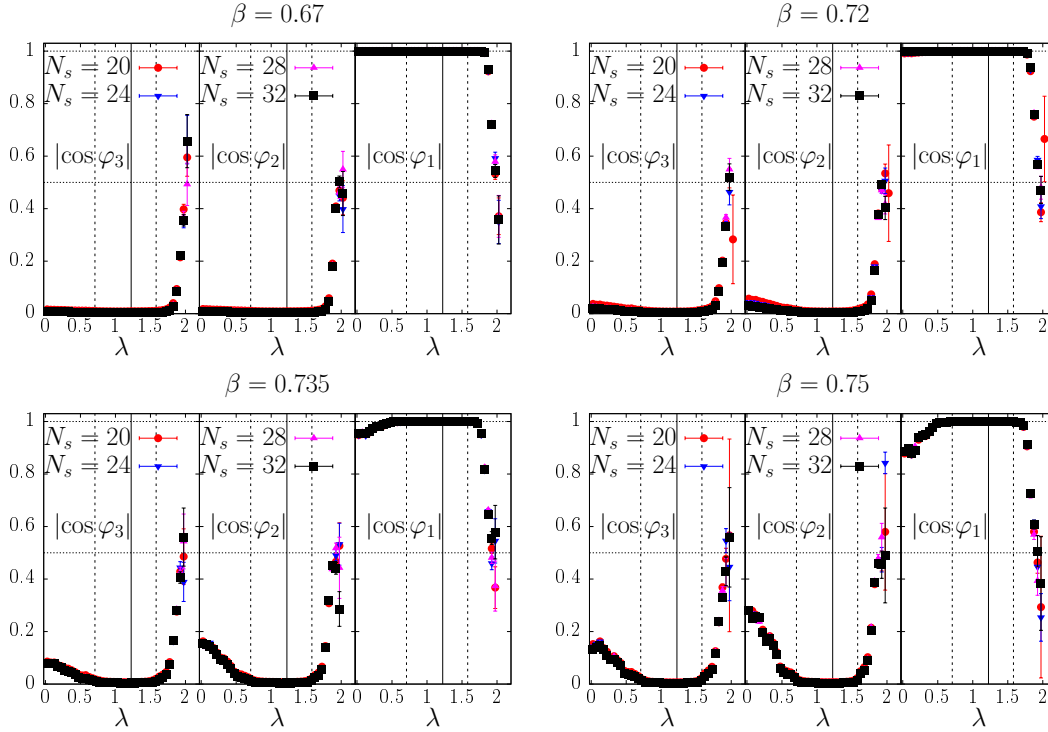


Figure 23: Confined (top row) and deconfined (bottom row) phase, physical sector: average orientation of the principal axes with respect to the time direction.

they are close to 2 but clearly deviate from it in the confined phase, taking values similar to those found in the physical sector.

**Mode shape** Information on the shape of the modes is summarized in Figs. 21 and 22. In the physical sector (Fig. 21), low modes become more and more rod-like/prolate as  $\beta$  increases. Bulk modes are instead slab-like/oblate, as expected for fully delocalized modes. High modes again tend to become more prolate as  $\beta$  increases, but they also become more spherical as one moves to higher  $\lambda$ . In the deconfined phase, this is a clear difference between the low localized modes and the high localized modes, the former being elongated while the latter are almost spherical. In the unphysical sector (Fig. 22), low modes are now slab-like/oblate, becoming more so as  $\beta$  increases. Bulk modes are again slab-like, fully delocalized, and high modes are again localized and almost spherical, with little difference between the two phases, and with the physical sector.

**Mode orientation** The average orientation of the modes with respect to the temporal direction (see right before Eq. (26)) is shown in Figs. 23 and 24. In the physical sector (Fig. 23), one finds for the low modes in the confined phase  $\langle \cos \varphi_3 \rangle \approx \langle \cos \varphi_2 \rangle \approx 0$  and

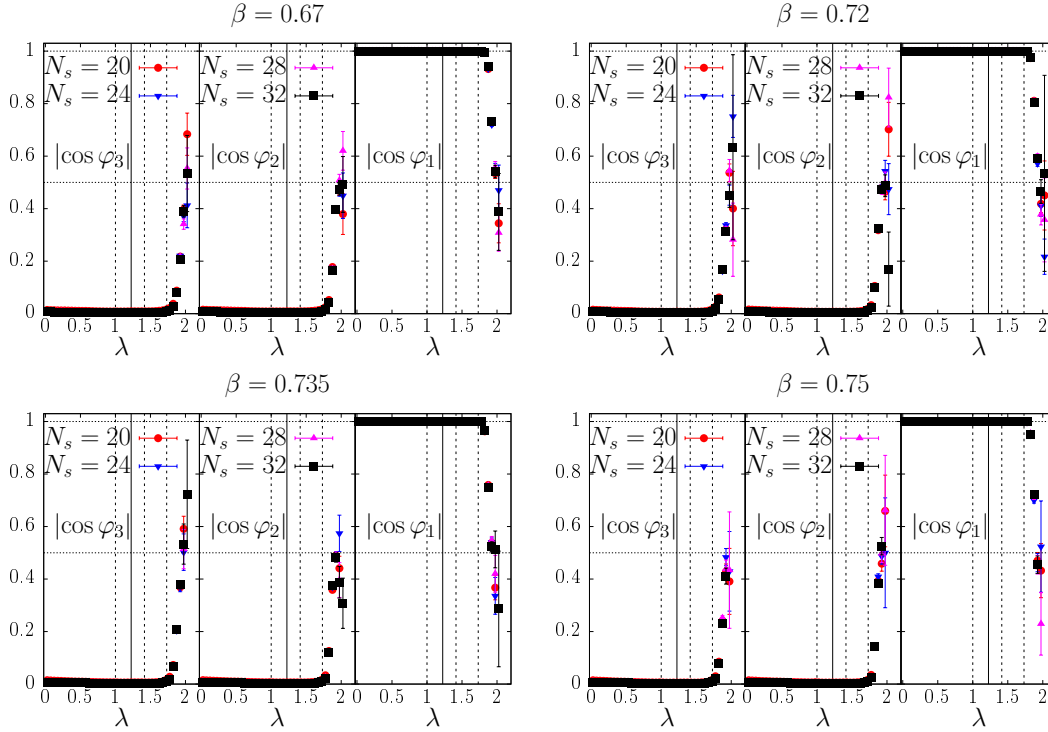


Figure 24: Confined (top row) and deconfined (bottom row) phase, unphysical sector: average orientation of the principal axes with respect to the time direction.

$\langle \cos \varphi_1 \rangle \approx 1$ , as expected for delocalized modes. Above the deconfinement transition, the deviations from 0 and 1 become much larger as the modes become localized, but they remain clearly away from  $\frac{1}{2}$ . This is consistent with the fact that they are typically not spherical but prolate, localized objects. For bulk modes one has  $\langle \cos \varphi_3 \rangle \approx \langle \cos \varphi_2 \rangle \approx 0$  and  $\langle \cos \varphi_1 \rangle \approx 1$  in both phases, as expected. For high modes  $\langle \cos \varphi_i \rangle \approx \frac{1}{2}$ , confirming that they are approximately spherical. In the unphysical sector (Fig. 24), the average orientation of low and bulk modes is again consistent with what one expects for delocalized modes, and that of high modes is again consistent with what one expects for spherical modes.

Overall, the results discussed above are consistent with the picture obtained from the participation ratio. In addition, they distinguish between the localized modes found at the low end (when present) and at the high end of the spectrum, that have different shapes.

**Characteristic lengths of low modes** Finally, in Fig. 25 we show the length scales  $\ell_i^{\text{phys}} = a l_i$  of the equivalent cuboid for the lowest modes ( $\lambda \in [0, \Delta\lambda]$ ) and the largest system size ( $N_s = 32$ ). More precisely, in Fig. 25 (top) we show the ratio  $\ell_3/N_t = \ell_3^{\text{phys}} T$ ,

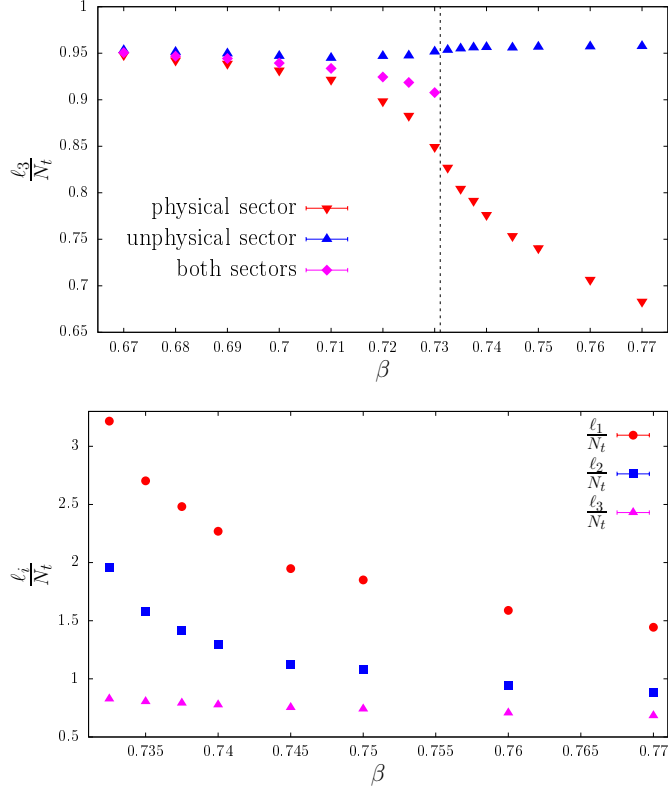


Figure 25: Top panel: temporal length scale  $\ell_3$  of the lowest modes in units of the inverse temperature in all phases/sectors. Bottom panel: length scales  $\ell_{1,2,3}$  of the lowest modes in units of the inverse temperature in the deconfined phase, physical sector.  $N_s = 32$  in both panels.

for all  $\beta$ s and sectors. This quantity is expected to have a finite thermodynamic limit, independently of the spatial localization properties of the modes, as it is expected to correspond essentially to the extension of the mode in the temporal direction. In Fig. 25 (bottom) we show instead  $\ell_{1,2,3}/N_t = \ell_{1,2,3}^{\text{phys}}T$  in the physical sector of the deconfined phase, which are again expected to have a finite thermodynamic limit due to the localized nature of the modes. The volume dependence is indeed mild, except for  $\ell_{1,2}^{\text{phys}}$  closer to  $\beta_c$ , where finite-size effects are still important. In particular,  $\ell_3^{\text{phys}}$  is of the same order of  $1/T$  for all  $\beta$ . In the deconfined phase, in the physical (resp. unphysical) sector it becomes smaller (resp. larger) than in the confined phase, indicating a reduced (resp. increased) extension in the temporal direction. In the physical sector in the deconfined phase, all the length scales  $\ell_i^{\text{phys}}$  are of the order of the inverse temperature.

## 5 Conclusions and outlook

The finite-temperature deconfinement transition of gauge theories leads to the appearance of localized Dirac modes at the low end of the spectrum in a variety of gauge theories, both in 3+1 [6–18, 20–22] and 2+1 [19, 26] dimensions. This has been put in a relation with the ordering of the Polyakov loop in the deconfined phase, and the formation of “islands” of fluctuations in the “sea” of ordered Polyakov loops, which are expected to be the localization centers for the low Dirac modes [16, 23–25]. This leads one to generally expect localization of the low Dirac eigenmodes in the high-temperature, deconfined phase of a gauge theory (in the physical center sector).

In this paper we have studied the localization properties of the eigenmodes of the staggered Dirac operator in the background of  $\mathbb{Z}_2$  gauge field configurations on the lattice in 2+1 dimensions. This is the simplest gauge theory displaying a deconfining transition at finite temperature, and so provides the most basic test of the “sea/islands” picture of localization. We have studied this theory by means of numerical simulations, producing full staggered spectra for configurations in both center sectors in order to study in detail the effects of the ordering of the Polyakov loop,  $P(\vec{x})$ , throughout the whole spectrum. Our numerical results confirm the predictions of the sea/islands picture: the low-lying Dirac modes, which are delocalized in the low-temperature phase, become localized in the high-temperature phase of the theory in the “physical” center sector selected by external fermion probes,  $\langle P(\vec{x}) \rangle > 0$ , displaying a strong correlation with the location of negative Polyakov loops. Instead, in the “unphysical” center sector selected by external pseudofermion probes,  $\langle P(\vec{x}) \rangle < 0$ , the low modes remain delocalized, and show a positive correlation with the location of positive Polyakov loops. Our results suggest that localization of the lowest modes in the physical sector takes place exactly at deconfinement, although a study on larger volumes is required to make a conclusive statement.

The available lattice sizes and accumulated statistics do not allow for a precise determination of the mobility edge separating the low-lying, localized modes and the bulk, delocalized modes in the deconfined phase of the theory in the physical sector. A dedicated study using larger lattices is required to determine the location of the mobility edge and understand better the nature of the corresponding Anderson transition, which is expected to be of BKT type. However, the existence of a mobility edge seems very likely, and there are indications of non-trivial scaling of eigenmodes in the bulk, expected for BKT-type Anderson transitions.

A novel result obtained in this paper is that the very high modes, near the upper end of the spectrum, are localized in both phases of the theory, irrespectively of the center sector. The localized nature of these modes can be understood similarly to that of the low modes in the physical sector at high temperature, if one recalls the “Dirac-Anderson” form of the staggered operator [24, 25]. In the Dirac-Anderson basis, the staggered operator looks like a set of  $N_t$  coupled Anderson models, with on-site “energies” provided by the phase  $\phi(\vec{x}) = 0, \pi$  of the Polyakov loop along the different “branches” of

the relation<sup>9</sup>  $\varepsilon_k(\vec{x}) = \sin \frac{(2k+1)\pi + \phi(\vec{x})}{N_t}$ ,  $k = 0, \dots, N_t - 1$ . Here for simplicity we take  $N_t$  to be a multiple of 4. If hopping terms are ignored, the “unperturbed” eigenstates are all spatially localized at the spatial points  $\vec{x}$  of the lattice. Moreover, when the phase of the Polyakov loop is  $\pi$ , two of the branches give 0 ( $k = \frac{N_t}{2} - 1$  and  $k = N_t - 1$ ), and another two branches give  $\pm 1$  ( $k = \frac{N_t}{4} - 1$  and  $k = \frac{3N_t}{4} - 1$ ) for the on-site energy of the corresponding Anderson model. When the phase of the Polyakov loop is 0, four of the branches give  $\pm \sin \frac{\pi}{N_t}$  ( $k = 0, \frac{N_t}{2} - 1$  and  $k = \frac{N_t}{2}, N_t - 1$ ), and other four of the branches give  $\pm \cos \frac{\pi}{N_t}$  ( $k = \frac{N_t}{4} - 1, \frac{N_t}{4}$  and  $k = \frac{3N_t}{4} - 1, \frac{3N_t}{4}$ ). When the effect of the hopping terms is taken into account, the localized unperturbed modes mix and tend to delocalize, but they have a chance of remaining localized if they are in a spectral region where the spectral density remains sufficiently small, so that mixing is reduced. Such regions can only be outside of the spectral range of the free 2+1 dimensional Dirac operator in the two center sectors (i.e., setting either  $U_1(N_t - 1, \vec{x}) \equiv 1$  or  $U_1(N_t - 1, \vec{x}) \equiv -1, \forall \vec{x}$ , and all other link variables to 1). While for the spectral region near zero this is the case only at large  $\beta$  in the physical sector, for the high end (and its symmetric reflection in the negative spectrum) this happens in both phases of the theory. In the deconfined phase in the physical sector, the rare sites where  $\phi = \pi$  are preferred by the localized modes, while in the unphysical sector only the rare sites with  $\phi = 0$  can support localization in the sea of  $\phi = \pi$  sites. It would be interesting to check whether the same situation is found in physically more relevant gauge theories, e.g., in QCD.

The correlation between low modes and positive Polyakov loops observed in the unphysical sector in the deconfined phase, while not explainable in terms of “energetically” favorable islands “attracting” the mode, is not in contrast with the sea/islands picture of localization. As pointed out in Ref. [24], an important effect of the ordering of Polyakov loops in the deconfined phase is that it induces a strong correlation between different time slices, that leads to the decoupling of the Anderson models mentioned above. Conversely, the reduced correlation in the confined phase is important for their mixing, which is needed for the accumulation of low modes and the consequent spontaneous breaking of chiral symmetry. In the unphysical sector above  $\beta_c$ , the correlation between time slices is locally reduced where the Polyakov loop fluctuates away from order, which in this case means that it takes the value +1. These locations are favorable for the different Anderson models to mix, which can lead to a lowering of the eigenvalue, and can explain the enhancement of the low modes near positive Polyakov loops.

We have also demonstrated that all localized modes display a strong correlation with the position of negative plaquettes, again in both phases of the theory and irrespectively of the center sector. This is not entirely surprising, given the above-mentioned correlation of localized modes with Polyakov loops, and the correlation expected between Polyakov loop fluctuations and clusters of negative plaquettes. Nevertheless, the interplay between Polyakov loops, negative plaquettes, and localization of Dirac modes

---

<sup>9</sup>Here the temporal direction is taken to be direction 1, so that the corresponding staggered phase entering  $\varepsilon_k(\vec{x})$  is just  $\eta_1(x) = 1$ .

certainly deserves to be studied in more detail, as it may shed light on the mechanisms of the confinement/deconfinement transition and of localization of the low modes.

This work provides further confirmation of the close connection between localization of the low Dirac modes and deconfinement in finite-temperature gauge theories. Given the extreme simplicity of the model, there remains little doubt concerning the universality of this connection. A possible loose end may seem the case of gauge theories that display a deconfinement transition but whose gauge group has a trivial center, in which case the finite-temperature transition clearly cannot be associated with the spontaneous breaking of center symmetry. Localization of Dirac modes has not been studied yet in such theories, and so it is not clear whether it is present or not. In this case it may seem difficult to identify islands of Polyakov loop fluctuations. However, the sea/islands picture, as can be seen most easily making use of the Dirac-Anderson form of the staggered operator, favors localization on sites where the phase of one of the eigenvalues of the Polyakov loop is close to  $\pm\pi$ , irrespectively of whether this corresponds to a center element, or whether a nontrivial center even exists at all. It may then be worth studying the  $\mathbb{Z}_3$  gauge theory as well, where the center is not trivial but the Polyakov loop phase cannot get closer to  $\pm\pi$  than  $\pm\frac{2\pi}{3}$ . We hope that these kind of studies can help to shed more light on the mechanisms responsible for the deconfinement transition in finite-temperature gauge theories.

## Acknowledgments

We thank T. G. Kovács for useful discussions and a careful reading of the manuscript. MG was partially supported by the NKFIH grant KKP-126769.

## A IPR for degenerate eigenspaces

Suppose to have an  $n$ -fold degenerate eigenvalue of some Hermitian Hamiltonian  $H$ , describing a system living on a finite lattice, and let  $\{\psi_1(x), \dots, \psi_n(x)\}$  be an orthonormal basis of the corresponding eigenspace, with  $x$  denoting the lattice sites. It is easy to see that the IPR,  $\text{IPR} = \sum_x |\psi(x)|^4$ , is not constant over the vectors of unit norm,  $\sum_x |\psi(x)|^2 = 1$ , belonging to this eigenspace. Since no such vector is *a priori* singled out, it seems more appropriate to assign an average IPR to the whole eigenspace by averaging over all possible vectors of unit norm. The most general such vector can be obtained as a linear combination of basis vectors as  $\psi_a^U(x) = \sum_{i=1}^n U_{ai} \psi_i(x)$ , where  $U_{ai}$  are the entries of a unitary  $n \times n$  matrix. Here  $a$  can be fixed to any value  $a = 1, \dots, n$ , and it is only included for notational convenience; the final result should be independent of it. One has for the mode  $\psi_a^U$

$$\text{IPR}_a(U) = \sum_x |\psi_a^U(x)|^4 = \sum_x \sum_{i,j,k,l=1}^n U_{ai} \psi_i(x) U_{aj}^* \psi_j(x)^* U_{ak} \psi_k(x) U_{al}^* \psi_l(x)^*. \quad (32)$$

The average over all unit-norm vectors is obtained by group integration over  $U$  with the  $U(n)$  invariant (Haar) measure,  $dU$ . To this end, we will need the following results [65],

$$\begin{aligned} \int dU U_{ij} U_{kl}^{-1} &= \text{Wg}((1), n) \delta_{il} \delta_{jk}, \\ \int dU U_{ij} U_{kl}^{-1} U_{mn} U_{pq}^{-1} &= \text{Wg}((1, 1), n) (\delta_{il} \delta_{jk} \delta_{mq} \delta_{np} + \delta_{iq} \delta_{jp} \delta_{ml} \delta_{nk}) \\ &\quad + \text{Wg}((2), n) (\delta_{il} \delta_{jp} \delta_{mq} \delta_{nk} + \delta_{iq} \delta_{jk} \delta_{ml} \delta_{np}), \end{aligned} \quad (33)$$

where  $\text{Wg}(\cdot, n)$  is the Weingarten function for the unitary group, and

$$\text{Wg}((1), n) = \frac{1}{n}, \quad \text{Wg}((1, 1), n) = \frac{1}{n^2 - 1}, \quad \text{Wg}((2), n) = -\frac{1}{n(n^2 - 1)}. \quad (34)$$

It is now straightforward to obtain

$$\begin{aligned} \int dU \text{IPR}_a(U) &= \sum_x \sum_{i,j,k,l=1}^n \psi_i(x) \psi_j(x)^* \psi_k(x) \psi_l(x)^* \int dU U_{ai} U_{ja}^\dagger U_{ak} U_{la}^\dagger \\ &= \sum_x \sum_{i,j,k,l=1}^n \psi_i(x) \psi_j(x)^* \psi_k(x) \psi_l(x)^* \\ &\quad \times \left[ \frac{1}{n^2 - 1} (\delta_{ij} \delta_{kl} + \delta_{il} \delta_{jk}) - \frac{1}{n(n^2 - 1)} (\delta_{il} \delta_{kj} + \delta_{ij} \delta_{kl}) \right] \\ &= \frac{2}{n(n+1)} \sum_x \left( \sum_i |\psi_i(x)|^2 \right)^2. \end{aligned} \quad (35)$$

This is independent of  $a$ , and manifestly invariant under a unitary change of basis, as it should be: indeed,  $\sum_{i=1}^n |\psi_i(x)|^2 = E(x, x)$  equals the diagonal element of the projector  $E(x, y)$  over the degenerate eigenspace.

It is useful to notice that for quantities of the form

$$O_i = \sum_x O(x) |\psi_i(x)|^2 \quad (36)$$

it is sufficient to average the observables over a set of basis vectors for any orthonormal basis to automatically obtain the average of the observable over the whole degenerate eigenspace. In fact, setting

$$O_a(U) = \sum_x O(x) |\psi_a^U|^2 = \sum_x O(x) \sum_{i,j=1}^n U_{ai} U_{aj}^* \psi_i(x) \psi_j(x)^*, \quad (37)$$

and repeating the same procedure as above, one finds

$$\begin{aligned} \int dU O_a(U) &= \sum_x O(x) \sum_{i,j=1}^n \psi_i(x) \psi_j(x)^* \int dU U_{ai} U_{aj}^* \\ &= \sum_x O(x) \sum_{i,j=1}^n \psi_i(x) \psi_j(x)^* \frac{1}{n} \delta_{ij} = \frac{1}{n} \sum_x O(x) \left( \sum_{i=1}^n |\psi_i(x)|^2 \right), \end{aligned} \quad (38)$$

which is manifestly  $a$ - and basis-independent.

## References

- [1] T. Banks and A. Casher, Nucl. Phys. B **169**, 103 (1980).
- [2] V. Dick, F. Karsch, E. Laermann, S. Mukherjee, and S. Sharma, Phys. Rev. D **91**, 094504 (2015) [arXiv:1502.06190].
- [3] H. T. Ding, S. T. Li, S. Mukherjee, A. Tomiya, X. D. Wang, and Y. Zhang, Phys. Rev. Lett. **126**, 082001 (2021) [arXiv:2010.14836].
- [4] O. Kaczmarek, L. Mazur, and S. Sharma, *Eigenvalue spectra of QCD and the fate of  $U_A(1)$  breaking towards the chiral limit* (2021), arXiv:2102.06136.
- [5] A. Patella, Phys. Rev. D **86**, 025006 (2012) [arXiv:1204.4432].
- [6] A. M. García-García and J. C. Osborn, Phys. Rev. D **75**, 034503 (2007) [arXiv:hep-lat/0611019].
- [7] T. G. Kovács and F. Pittler, Phys. Rev. D **86**, 114515 (2012) [arXiv:1208.3475].
- [8] M. Giordano, T. G. Kovács, and F. Pittler, Phys. Rev. Lett. **112**, 102002 (2014) [arXiv:1312.1179].
- [9] G. Cossu and S. Hashimoto, J. High Energy Phys. **06**, 056 (2016) [arXiv:1604.00768].
- [10] L. Holicki, E.-M. Ilgenfritz, and L. von Smekal, PoS **LATTICE2018**, 180 (2018) [arXiv:1810.01130].
- [11] M. Göckeler, P. E. L. Rakow, A. Schäfer, W. Söldner, and T. Wettig, Phys. Rev. Lett. **87**, 042001 (2001) [arXiv:hep-lat/0103031].
- [12] C. Gattringer, M. Göckeler, P. E. L. Rakow, S. Schaefer, and A. Schäfer, Nucl. Phys. B **618**, 205 (2001) [arXiv:hep-lat/0105023].
- [13] R. V. Gavai, S. Gupta, and R. Lacaze, Phys. Rev. D **77**, 114506 (2008) [arXiv:0803.0182].

- [14] T. G. Kovács, Phys. Rev. Lett. **104**, 031601 (2010) [arXiv:0906.5373].
- [15] T. G. Kovács and F. Pittler, Phys. Rev. Lett. **105**, 192001 (2010) [arXiv:1006.1205].
- [16] F. Bruckmann, T. G. Kovács, and S. Schierenberg, Phys. Rev. D **84**, 034505 (2011) [arXiv:1105.5336].
- [17] M. Giordano, S. D. Katz, T. G. Kovács, and F. Pittler, J. High Energy Phys. **02**, 055 (2017) [arXiv:1611.03284].
- [18] T. G. Kovács and R. Á. Vig, Phys. Rev. D **97**, 014502 (2018) [arXiv:1706.03562].
- [19] M. Giordano, J. High Energy Phys. **05**, 204 (2019) [arXiv:1903.04983].
- [20] R. Á. Vig and T. G. Kovács, Phys. Rev. D **101**, 094511 (2020) [arXiv:2001.06872].
- [21] C. Bonati, M. Cardinali, M. D’Elia, M. Giordano, and F. Mazziotti, Phys. Rev. D **103**, 034506 (2021) [arXiv:2012.13246].
- [22] A. M. García-García and J. C. Osborn, Nucl. Phys. A **770**, 141 (2006) [arXiv:hep-lat/0512025].
- [23] M. Giordano, T. G. Kovács, and F. Pittler, J. High Energy Phys. **04**, 112 (2015) [arXiv:1502.02532].
- [24] M. Giordano, T. G. Kovács, and F. Pittler, J. High Energy Phys. **06**, 007 (2016) [arXiv:1603.09548].
- [25] M. Giordano, T. G. Kovács, and F. Pittler, Phys. Rev. D **95**, 074503 (2017) [arXiv:1612.05059].
- [26] F. Bruckmann and J. Wellenhofer, EPJ Web Conf. **175**, 07005 (2018) [arXiv:1710.05662].
- [27] P. W. Anderson, Phys. Rev. **109**, 1492 (1958).
- [28] D. J. Thouless, Phys. Rep. **13**, 93 (1974).
- [29] P. A. Lee and T. V. Ramakrishnan, Rev. Mod. Phys. **57**, 287 (1985).
- [30] F. Evers and A. D. Mirlin, Rev. Mod. Phys. **80**, 1355 (2008) [arXiv:0707.4378].
- [31] E. Abrahams, ed., *50 Years of Anderson Localization*, (World Scientific, Singapore, 2010).
- [32] S. M. Nishigaki, M. Giordano, T. G. Kovács, and F. Pittler, PoS **LATTICE2013**, 018 (2014) [arXiv:1312.3286].

- [33] L. Ujfalusi, M. Giordano, F. Pittler, T. G. Kovács, and I. Varga, *Phys. Rev. D* **92**, 094513 (2015) [arXiv:1507.02162].
- [34] A. M. García-García and E. Cuevas, *Phys. Rev. B* **74**, 113101 (2006) [arXiv:cond-mat/0602331].
- [35] T. Takaishi, K. Sakakibara, I. Ichinose, and T. Matsui, *Phys. Rev. B* **98**, 184204 (2018) [arXiv:1808.03419].
- [36] T. Wang, T. Ohtsuki, and R. Shindou, *Phys. Rev. B* **104**, 014206 (2021) [arXiv:2105.02500].
- [37] F. J. Wegner, *J. Math. Phys. (N.Y.)* **12**, 2259 (1971).
- [38] R. Balian, J. M. Drouffe, and C. Itzykson, *Phys. Rev. D* **11**, 2098 (1975).
- [39] J. B. Kogut, *Rev. Mod. Phys.* **51**, 659 (1979).
- [40] R. Á. Vig and T. G. Kovács, *Phys. Rev. D* **103**, 114510 (2021) [arXiv:2101.01498].
- [41] D. Scheffler, C. Schmidt, D. Smith, and L. von Smekal, *PoS LATTICE2013*, 191 (2014) [arXiv:1311.4324].
- [42] M. Caselle and M. Hasenbusch, *Nucl. Phys. B* **470**, 435 (1996) [arXiv:hep-lat/9511015].
- [43] C. Burden and A. Burkitt, *Europhys. Lett.* **3**, 545 (1987).
- [44] E. Abrahams, P. W. Anderson, D. C. Licciardello, and T. V. Ramakrishnan, *Phys. Rev. Lett.* **42**, 673 (1979).
- [45] X. C. Xie, X. R. Wang, and D. Z. Liu, *Phys. Rev. Lett.* **80**, 3563 (1998).
- [46] E. König, P. Ostrovsky, I. Protopopov, and A. Mirlin, *Phys. Rev. B* **85**, 195130 (2012) [arXiv:1201.6288].
- [47] K. Slevin and T. Ohtsuki, *Phys. Rev. B* **80**, 041304 (2009) [arXiv:0905.1163].
- [48] M. R. Zirnbauer, *Nucl. Phys. B* **941**, 458 (2019) [arXiv:1805.12555].
- [49] E. J. Dresselhaus, B. Sbierski, and I. A. Gruzberg, *Ann. Phys. (Amsterdam)* **431**, 168560 (2021) [arXiv:2101.01716].
- [50] Y.-Y. Zhang, J. Hu, B. A. Bernevig, X. R. Wang, X. C. Xie, and W. M. Liu, *Phys. Rev. Lett.* **102**, 106401 (2009) [arXiv:0810.1996].
- [51] M. L. Mehta, *Random matrices*, Vol. 142, , 3 ed. (Elsevier, New York, 2004).

- [52] J. J. M. Verbaarschot and T. Wettig, *Annu. Rev. Nucl. Part. Sci.* **50**, 343 (2000) [arXiv:hep-ph/0003017].
- [53] C. Soukoulis, I. Webman, G. S. Grest, and E. N. Economou, *Phys. Rev. B* **26**, 1838 (1982).
- [54] A. Eilmes, R. A. Römer, and M. Schreiber, *Eur. Phys. J. B* **1**, 29 (1998) [arXiv:cond-mat/9706265].
- [55] S.-J. Xiong and S. N. Evangelou, *Phys. Rev. B* **64**, 113107 (2001) [arXiv:cond-mat/0101135].
- [56] L. Schweitzer and P. Markoš, *Phys. Rev. B* **85**, 195424 (2012) [arXiv:1204.0621].
- [57] O. Motrunich, K. Damle, and D. A. Huse, *Phys. Rev. B* **65**, 064206 (2002) [arXiv:cond-mat/0107582].
- [58] F. Gliozzi, M. Panero, and P. Provero, *Phys. Rev. D* **66**, 017501 (2002) [arXiv:hep-lat/0204030].
- [59] L. Bai and D. Breen, *J. Graph. Tools* **13**, 53 (2008).
- [60] E. Anderson, Z. Bai, C. Bischof, S. Blackford, J. Demmel, J. Dongarra, J. Du Croz, A. Greenbaum, S. Hammarling, A. McKenney, and D. Sorensen, *LAPACK Users' Guide*, (SIAM, Philadelphia, 1999).
- [61] A. Alexandru and I. Horváth, *Phys. Rev. Lett.* **127**, 052303 (2021) [arXiv:2103.05607].
- [62] M. Giordano, *J. Phys. A* **54**, 37LT01 (2021) [arXiv:2009.00486].
- [63] A. J. McKane and M. Stone, *Ann. Phys. (N.Y.)* **131**, 36 (1981).
- [64] M. Golterman and Y. Shamir, *Phys. Rev. D* **68**, 074501 (2003) [arXiv:hep-lat/0306002].
- [65] B. Collins, *Int. Math. Res. Not.* **2003**, 953 (2003) [arXiv:math-ph/0205010].